UC Irvine
UC Irvine Previously Published Works

Title

Presynaptic Homeostasis Opposes Disease Progression in Mouse Models of ALS-Like Degeneration: Evidence for Homeostatic Neuroprotection

Permalink

https://escholarship.org/uc/item/0xp1j5rm

Journal

Neuron, 107(1)

ISSN

0896-6273

Authors

Orr, Brian O
Hauswirth, Anna G
Celona, Barbara
et al.

Publication Date

2020-07-01

DOI

10.1016/j.neuron.2020.04.009

Peer reviewed

Presynaptic Homeostasis Opposes Disease Progression in Mouse Models of ALS-Like Degeneration: Evidence for Homeostatic Neuroprotection

Brian O. Orr[1,6], **Anna G. Hauswirth**[1,6], **Barbara Celona**[2], **Richard D. Fetter**[1], **Giulia Zunino**[1], **Evgeny Z. Kvon**[3], **Yiwen Zhu**[3], **Len A. Pennacchio**[3,4,5], **Brian L. Black**[2], **Graeme W. Davis**[1,7]

[1.]Department of Biochemistry and Biophysics, Kavli Institute for Fundamental Neuroscience, University of California, San Francisco, CA 94941

[2.]Cardiovascular Research Institute, University of California, San Francisco, CA.

[3.]Environmental Genomics and Systems Biology Division, Lawrence Berkeley National Laboratory, Berkeley, CA, 94720, USA

[4.]U.S. Department of Energy Joint Genome Institute, Walnut Creek, CA 94598, USA

[5.]Comparative Biochemistry Program, University of California, Berkeley, CA 94720, USA

[6.]These authors contributed equally.

[7.]Lead Contact

SUMMARY

Progressive synapse loss is an inevitable and insidious part of age-related neurodegenerative disease. Typically, synapse loss precedes symptoms of cognitive and motor decline. This suggests the existence of compensatory mechanisms that can temporarily counteract the effects of ongoing neurodegeneration. Here, we demonstrate that presynaptic homeostatic plasticity (PHP) is induced at degenerating neuromuscular junctions, mediated by an evolutionarily conserved activity of presynaptic ENaC channels in both *Drosophila* and mouse. To assess the consequence of eliminating PHP in a mouse model of ALS-like degeneration, we generated a motoneuron-specific deletion of *Scnn1a*, encoding the ENaC channel alpha subunit. We show that *Scnn1a* is essential for PHP without adversely affecting baseline neural function or lifespan. However, *Scnn1a* knockout in a degeneration-causing mutant background accelerated motoneuron loss and disease progression to twice the rate observed in littermate controls with intact PHP. We propose a model of neuroprotective homeostatic plasticity, extending organismal lifespan and health-span.

ETOC:

Synapse loss is an insidious aspect of aging and neurodegenerative disease, typically preceding symptoms of cognitive or motor decline. Orr et al., define a conserved mechanism of homeostatic plasticity (*Drosophila* and mice) that sustains neural function during an early phase of neuromuscular degenerative disease, underscoring a model of 'homeostatic neuroprotection'.

INTRODUCTION

In both normal individuals and those afflicted by neurodegenerative diseases such as amyotrophic lateral sclerosis (ALS), profound synapse loss can occur prior to the onset of symptomatic cognitive or motor decline (Fearnley and Lees, 1991; Moloney et al., 2014; Morrison and Baxter, 2012; Peters et al., 2008). One possible explanation for symptomatic delay is that homeostatic signaling mechanisms initially act to counteract the deleterious effects of synapse loss. However, there remains little direct evidence that homeostatic plasticity is induced by neurodegeneration and it remains unknown whether homeostatic plasticity will have beneficial effects on the rate of disease progression, health-span or lifespan.

There has been tremendous progress defining the molecular and genetic underpinnings of ALS in human, leading to an explosion of research and new animal models (Price et al., 1994; LaMonte et al., 2002; Taylor et al., 2016; Figley and Gitler, 2013; McGurk, et al., 2015; Cook and Petrucelli, 2019; Petel Légaré et al., 2019; Estes et al., 2013; Graf et al., 2011; Klim et al., 2019; Melamed et al., 2019). Based on these ALS models, it has become clear that disease progression at the NMJ is dynamic (Chand et al., 2018; Filipchuk and Durand, 2012; Yuva-Aydemir et al., 2018). Anatomically, neuromuscular and dendritic remodeling can precede NMJ elimination (Shaefer et al., 2005; Martineau et al., 2018; Fillipchuk and Durand, 2012). In other instances, a potentiation of spontaneous neurotransmission has been documented (Bose et al., 2019; Dzieciolowska et al., 2019) and there is evidence of elevated motoneuron excitation and excitability (Petel Légaré et al., 2019; for review; Starr and Sattler, 2018). But, once again, there remains no direct evidence that these events are homeostatic in nature, nor is there evidence that these functional correlates are beneficial to the diseased organism.

Presynaptic homeostatic plasticity (PHP) is a potent adaptive physiological mechanism that stabilizes information transfer at synaptic connections, with an effect size that can exceed 200–500% at human, mouse and insect NMJ (Cull-Candy et al., 1980; Davis, 2013, 2006; Plomp et al., 1992; Sons et al., 2003). PHP has been demonstrated to offset large deficits in postsynaptic neurotransmitter receptor number or function, and several studies have inferred the existence of PHP at degenerating neuromuscular synapses. For example, synaptic gain is maintained at wild type levels despite profound neuromuscular degeneration in *Drosophila* (Pielage et al., 2005), and PHP can be experimentally induced at a degenerating NMJ (Perry et al., 2017). But, it remains unknown whether PHP is actually induced by the process of synapse disassembly. Establishing whether or not neurodegeneration induces the expression of homeostatic plasticity requires the blockade of homeostatic plasticity and subsequent demonstration that degenerating synapses are differentially affected compared to controls.

Here we achieve this goal, ultimately providing evidence of homeostatic neuroprotection in a mammalian model of ALS-like neuromuscular disease.

RESULTS

The phenomenon of PHP is conserved from fly to human at the NMJ (Cull-Candy et al., 1980; Sons et al., 2003; Younger et al., 2013). We began our work at the *Drosophila* NMJ where we have a demonstrated ability to induce neurodegeneration and pharmacologically control the expression of PHP.

PHP sustains synaptic transmission at degenerating NMJ

We previously developed an assay that is now widely used to visualize and quantify neuromuscular degeneration at the *Drosophila* NMJ. This assay is based on the observation that degeneration of the presynaptic motoneuron terminal occurs more rapidly than the loss of postsynaptic markers. Therefore, the severity of NMJ degeneration can be precisely quantified by determining the number of presynaptic boutons that are eliminated compared to those that are retained at any given NMJ (Eaton et al., 2002; Keller et al., 2011; Massaro et al., 2009; Pielage et al., 2008, 2005). Our initial goal was not to model ALS in *Drosophila*, but to take advantage of genetic mutations that cause profound neuromuscular degeneration, allowing us to clearly assess the relationship between degeneration and PHP.

The Drosophila *ankyrin2* gene encodes a giant Ankyrin that, when deleted, causes profound NMJ degeneration, inclusive of complete NMJ elimination (Pielage et al., 2008; Massaro et al., 2009). An example of partial NMJ degeneration in the *ank2* mutant is shown in Figure 1A. At sites of ongoing NMJ degeneration, well-formed clusters of neurotransmitter receptors (anti-GluRIIC) can be observed that lack juxtaposed presynaptic release sites (anti-BRP), imaged using super-resolution microscopy (see methods). These data are quantitatively similar to previously published analyses (Pielage et al., 2008; Massaro et al., 2009; Keller et al., 2011).

We recorded from degenerating NMJ in the *ank2* mutation. Then, for each individual recording, we retrospectively quantified the extent of degeneration. Synaptic efficacy was sustained at wild type levels until >40% of the NMJ degenerated (Figure 1B), replicating observations at NMJ depleted of presynaptic *Spectrin* (Pielage et al., 2005). The maintenance of wild type synaptic transmission could reflect some form of redundancy or safety factor (Marrus and DiAntonio, 2005), or could reflect the induction of PHP. To distinguish among these possibilities, we asked whether blocking PHP had a disproportionately large effect at degenerating nerve terminals.

A presynaptic epithelial sodium channel (ENaC) orthologue is essential for the expression of PHP at the *Drosophila* NMJ and can be blocked by acute administration of benzamil (Orr et al., 2017; Younger et al., 2013). We confirmed that benzamil has no effect on neurotransmitter release at the wild type NMJ (Figure 1C, D; Younger et al., 2013; Orr et al., 2017: Note that Supplemental Tables S1 and S2 include values for graphs that lack individual data points).

To determine the effect of benzamil at degenerating nerve terminals, we visualized NMJ integrity using a vital stain and selected NMJ undergoing degeneration based on the appearance of a discontinuous presynaptic membrane (see methods). The selection procedure had no effect on average baseline transmission, demonstrated by the fact that selected NMJ have wild type levels of baseline neuromuscular transmission (Figure 1C, "-Benz"). Since degeneration is present, but synaptic transmission is normal, we conclude that our selection identifies NMJ that are in the early stages of degeneration, encompassing between 20% and 40% of the NMJ (comparison with Figure 1A), consistent with a clearly visible, but fragmented presynaptic nerve terminal membrane. Subsequent application of benzamil (thereby blocking PHP) caused a profound decrease in presynaptic neurotransmitter release, an effect that was only observed at degenerating *ank2* NMJ (Figure 1C, "+ Benz"). Importantly, the benzamil effect rapidly reversed upon a 10-minute washout (Figure 1C, wash). The same data are re-plotted in Figure 1D, showing the relationship between quantal content (average number of vesicles released per action potential) prior to and following benzamil application. Wild type NMJ recordings reside close to the line of unity, whereas all but one of the *ank2* NMJ recordings reside substantially below unity.

Next, we addressed possible concerns regarding the selection of degenerating NMJ and repeated our experiment, with a larger sample size, blindly recording from all NMJ, of which approximately 65% will have ongoing degeneration of varying severity (Keller et al., 2011; Pielage et al., 2008). In wild type, benzamil application drives a small increase in average quantal content of unknown origin (Figure 1E). By contrast, benzamil caused a significant decrease in quantal content in the *ank2* mutant, with some NMJ showing almost complete functional blockade (Figure 1F).

The long-term induction of PHP at the *Drosophila* NMJ correlates with increased transcription and translation of the three essential ENaC channel subunits (*ppk1*, *ppk11* and *ppk16*) in motoneurons (Orr et al., 2017; Younger et al., 2013). We reasoned a similar effect would be observed during progressive NMJ degeneration. Indeed, quantitative RT-PCR revealed that the ENaC channel subunits *ppk11* and *ppk16* have significantly increased expression in the CNS of the *ank2* mutant compared to control (99% increase, 19.59% SEM; three biological, six technical replicates; Table S3).

To determine whether anatomical degeneration was the event that caused the induction of PHP, we suppressed anatomical degeneration in the *ank2* mutant by deleting the executioner caspase *dcp-1* (Keller et al., 2011). First, we confirmed complete suppression of degeneration in the *ank2; dcp-1* double mutant. Then, we demonstrated that application of benzamil had no effect on quantal content in *ank2; dcp-1* double mutants (Figure 1G, H), arguing that anatomical neurodegeneration, not the *ank2* mutation *per se*, is responsible for the induction of PHP.

It was previously demonstrated that mEPSP amplitudes often remain unchanged during neuromuscular degeneration in *Drosophila* (Eaton et al., 2002). Given this, we asked whether the induction of PHP in *ank2* occludes any further expression of PHP caused by application of philanthotoxin (PhTX). It does not (Figure 1I, J). Note that baseline quantal content is significantly lower in the *ank2* mutant compared to wild type, consistent with a

large fraction of recorded NMJ experiencing substantive degeneration (>40% loss of the NMJ; Figure 1B). None-the-less, the average magnitude of PHP expression was as large as that observed in wild type (Figure 1J), demonstrating that ongoing neurodegeneration does not occlude further induction of PHP.

Neuromuscular degeneration induces expression of PHP in mice

We sought to translate our findings to mammalian models of ALS-like degeneration. To do so, we used two previously published mouse models. The first model (Prp-*TDP43^{A315T}*; hereafter simply referred to as *TDP-43* for simplicity) involves expression of a mutant isoform of the TDP-43 protein (Neumann et al., 2006; Van Deerlin et al., 2008; Gitcho et al., 2008). This mouse model causes a phenotype of progressive, age-dependent neuromuscular degeneration and severely reduced lifespan (Wegorzewska et al., 2009). The second model is based on a gene knockout. The *Zfp106* knockout mouse exhibits progressive motoneuron death, NMJ degeneration and age-dependent progressive paralysis (Joyce et al., 2016; Anderson et al., 2016; Celona *et al.*, 2017). Although the *Zfp106* gene mutation has not been identified in human patients, we use this model as a second, distinct, loss-of-function genetic model to study ALS-like degeneration in mice.

We first confirmed NMJ degeneration at the *TDP-43* mouse diaphragm muscle (Figure 2A). Data were acquired at postnatal day 65–70 (P65–70), following phenotypic onset, including defects in grasping, hind limb strength and motility, just prior to end stage (end stage is defined as the time at which euthanasia is required, determined by body condition and well-being as stated in methods). In *TDP-43* animals, the major branch of the phrenic nerve was still evident based on neurofilament staining. Endplate bands in *TDP-43* animals were of similar width compared to wild type (Figure 2A), but showed widespread evidence of endplate denervation (Figure 2A, inset). Degeneration at individual NMJ endplates was defined by staining for three antigens; 1) anti-Neurofilament, 2) synaptic vesicles (anti-SV2; see Supplemental Figure 1) and 3) acetylcholine receptors (AChR) (Figure 2). Degeneration was scored based upon the degree to which the neurofilament and anti-SV2 staining was fragmented or diminished when visualized in opposition to AChR clusters (Figure 2B and Supplemental Figure 1). Based on these criteria, we observe that 30% of NMJ are undergoing anatomical degeneration at this stage. This level of degeneration is consistent with prior characterization of a different TDP-43 mouse model (*TDP-43^{Q311K}*) where 30% endplate degeneration was documented (Ditsworth et al., 2017) and consistent with degeneration levels observed in *SOD1* mice (Shaefer et al,. 2005). We also assessed the extent of degeneration by electrophysiological recordings. At this stage, 7% of NMJ were electrophysiologically silent, having normal resting potential and input resistance, but no evidence of spontaneous mEPSPs or evoked neurotransmission (Figure 2C). We presume that this is evidence of complete synapse elimination at a subset of the NMJ undergoing anatomical degeneration.

Next, we assessed synaptic efficacy. Again, we assessed NMJ function at P65–70, just prior to end stage. We calculated average values for mEPP, EPP and quantal content, excluding complete synapse eliminations (defined as recordings with zero mEPPs or EPPs). All three estimates in *TDP-43* were equivalent to controls, despite widespread evidence of

degeneration at 30% of nerve terminals (Figure 2C). This electrophysiological analysis parallels our observations at the *Drosophila* NMJ (Figure 1), suggesting the presence of ongoing compensatory mechanisms that sustain NMJ function despite ongoing synapse disassembly.

Similar neuromuscular degeneration was observed in the homozygous *Zfp106* knockout mouse model. *Zfp106* mutant mice reach end stage and require euthanasia at approximately P90–100. Therefore, we assessed NMJ anatomy at ~P90, just prior to end stage. Compared to littermate controls, endplate bands in *Zfp106* knockouts were of similar width, but showed widespread evidence of endplate denervation (Figure 2D,E). Nearly 50% of all endplates showed evidence of severe degeneration (Figure 2F, far right graph). Furthermore, approximately 25% of NMJ were electrophysiologically silent, indicative of complete NMJ elimination. Interestingly, our anatomical analysis of degeneration in the *TDP-43* and *Zfp106* mutants reveals that synaptic degeneration proceeds, qualitatively, in slightly different ways in these two neurodegenerative models (Figure 2, Supplemental Figure 2).

The electrophysiological analysis of neurotransmission in the homozygous *Zfp106* knockout revealed an interesting difference compared to *TDP-43*, consistent with a degeneration-dependent induction of PHP in *Zfp106*. In the homozygous *Zfp106* mutant, we found a significant reduction in average mEPP amplitude, maintenance of nearly wild type EPP amplitudes and an associated increase in quantal content (Figure 2F, see also Supplemental Figure 3 A, B). We speculate that the observed decrease in clustered AChRs (Figure 2E and Supplemental Figure 1) may be responsible for the decrease in average mEPP amplitude and, thereby, induce a classical homeostatic increase in presynaptic release. This effect was not observed in *TDP-43*, perhaps reflecting putative differences in the speed of neuromuscular disassembly, where *Zfp106* NMJ might degrade more slowly, enabling recordings from NMJ with diminished AChRs, prior to complete elimination. Finally, we note that the presence and extent of NMJ degeneration appears independent of a change in mEPP frequency, consistent with previously published observations in another ASL mouse model (Supplemental Figure 4; Tremblay et al., 2017).

To determine whether the apparent induction of PHP, caused by decreased mEPP amplitude, is correlated with NMJ degeneration in the homozygous *Zfp106* mutant, we performed an analysis of synaptic transmission over the course of disease progression. Synaptic transmission was analyzed at three time points: P30 (prior to NMJ degeneration), P60 (onset of NMJ degeneration) and P90 (just prior to end stage). At P30, all measures of synaptic transmission remained similar to wild type. At P60, mEPP amplitudes were decreased and PHP was induced. At P90, mEPP amplitudes remained depressed and PHP was still evident. Thus, defects in mEPP amplitude and the induction of PHP correlate with the onset of NMJ degeneration (Supplemental Figure 3 C, D).

Finally, we supply additional electrophysiological evidence, suggesting that the induction of PHP in the *Zfp106* mutant is similar to the acute induction of PHP at the wild type NMJ. Induction of PHP at the wild type NMJ was achieved by application of a sub-blocking concentration curarine (0.1 μM), acutely inhibiting postsynaptic AChRs, as done previously (Wang et al., 2016) (Supplemental Figure 3A, B). After 10 minutes of curarine incubation,

decreased mEPP amplitudes are offset by a homeostatic increase in presynaptic release (Supplemental Figure 3A, B). We plotted wild type mEPP amplitude against quantal content (recordings made in the absence and presence of curarine) and observed a strong, statistically significant, negative correlation (Supplemental Figure 3A). When we superimposed data recorded from the *Zfp106* knockout we found that recordings from the mutant resided within the confidence interval that encompasses 95% of all wild type data (gray lines). Since the precise relationship between mEPP amplitude and quantal content is preserved in the *Zfp106* knockout, it suggests that classically defined PHP was induced at degenerating nerve terminals in the homozygous *Zfp106* knockout mouse. We note one further similarity comparing the induction of PHP at degenerating in *Drosophila* and mouse. As in *Drosophila*, degeneration-dependent induction of PHP does not occlude the further induction of PHP by application of curarine to the *Zfp106 KO* NMJ (Supplemental Figure 3E).

Evolutionarily Conserved ENaC-dependent mechanism of PHP at the mouse NMJ

Although the phenomenon of PHP is conserved from *Drosophila* to mouse and human NMJ (Cull-Candy et al., 1980; Sons et al., 2003; Younger et al., 2013), it remains unknown whether PHP is achieved by the same molecular mechanisms in *Drosophila* and mammals. The *Scnn1a* gene encodes an essential subunit of the mammalian ENaC channel, with high expression in the kidney and lung, but also with documented expression in the central brain and spinal cord (Dyka et al., 2005; Giraldez et al., 2013; Hummler et al., 1996; Teruyama et al., 2012). We hypothesized that ENaC channel function might mediate PHP at the mouse NMJ. As a first test of this hypothesis, we asked whether the ENaC channel antagonist (benzamil) blocks the acute induction of PHP at the mouse NMJ, as it does in *Drosophila*.

First, we demonstrate that application of curarine (0.1 μM) to the wild type NMJ induces the expression of PHP (Figure 3A), consistent with recent literature (Wang et al., 2016). Next, we demonstrate that application of benzamil to the wild type NMJ has no significant effect on the average EPP, or quantal content (Figure 3A). There is a modest reduction in mEPP amplitude, possibly paralleling a postsynaptic ENaC activity that is unrelated to PHP in Drosophila. However, when curarine is applied to an NMJ that had been pretreated with benzamil, then PHP is completely blocked (+Benz, +Cur in Figure 3A). We observed a curarine-dependent drop in mEPP amplitude without an increase in quantal content and, as a consequence, average EPP amplitude is severely decreased (Figure 3).

We also re-plot our data to illustrate the negative correlation between mEPP amplitude and quantal content for wild type NMJ recorded in the absence (filled black points) and presence (open black points) of curarine (Figure 3B). When NMJ are pre-incubated in benzamil (see methods), the negative correlation is blocked (Figure 3C). Taken together, these data demonstrate that acute application of benzamil blocks expression of PHP at the mouse NMJ, just as it does at the *Drosophila* NMJ (Orr et al., 2017; Younger et al., 2013). These data demonstrate a conserved, benzamil-sensitive mechanism of PHP at the mouse NMJ, most likely due to the action of presynaptic ENaC channels.

Conditional Scnn1a motoneuron-specific knockouts block PHP.

Scnn1a encodes an essential subunit of the mouse Deg/ENaC channel. We generated a conditional *Scnn1a* knockout (Figure 4A,C,D). When *Scnn1a$^{flox/flox}$* mice were bred to harbor a ubiquitous Cre driver (*UBC-ERT2-Cre/+*), the animals died at postnatal day P2, consistent with the lethal phenotype of conventional germline *Scnn1a* knockouts, which also die at postnatal day 2 (Hummler et al., 1996). Next, the *Scnn1a$^{flox/flox}$* animals were bred to harbor a Nestin-Cre driver that expresses Cre throughout the CNS. *Scnn1a$^{flox/flox}$*;*Nestin-Cre$^{Tg/0}$* mice demonstrate effective knockout of *Scnn1a* in the cortex, evaluated by qPCR (Supplemental Table S3). These experiments establish that *Scnn1a* expression can be effectively eliminated in *Scnn1a$^{flox/flox}$* mice in a Cre-dependent manner.

We bred animals harboring *Scnn1a$^{flox/flox}$* and *Mnx1$^{Cre/+}$* (hereafter referred to as HB9-Cre; see methods) to generate motoneuron-specific knockouts. This Cre driver is sufficient to eliminate *Scnn1a* expression in motoneurons without affecting muscle, allowing us to ascribe *Scnn1a* function to motoneurons (Arber et al., 1999). We refer to *Scnn1a$^{flox/flox}$*;*HB9^{Cre}* mice as *Scnn1a-CKO* (conditional knockout).

Scnn1a-CKO mice were born in normal numbers, had normal weight and, to date, have an apparently normal lifespan in excess of one year (Figure 4B, and see below). The anatomy and synaptic transmission measured in the *Scnn1a-CKO* diaphragm muscle are essentially normal (Figure 4E–H; see also below). However, when a sub-blocking concentration of curarine was applied to the NMJ to inhibit AChRs, we found that the expression of PHP was completely blocked (Figure 4H). We conclude that Scnn1a is an evolutionarily conserved effector for PHP at the mouse NMJ. It is notable that the *Drosophila* NMJ utilizes glutamate as a neurotransmitter, while the mouse NMJ utilizes acetylcholine. Regardless, the same conserved mechanism of PHP is expressed at these biochemically distinct NMJ, arguing for the evolutionarily ancient origins of PHP at the NMJ.

Finally, we note minor effects in *Scnn1a-CKO* on baseline neurotransmission. Baseline EPP amplitudes were slightly, but significantly, decreased when *Scnn1a-CKO* were compared to littermate controls. There were also small differences in mEPP amplitudes. However, calculation of quantal content showed no significant difference comparing controls and the *Scnn1a-CKO* (Figure 5H). It should also be noted that we attempted to define the presence of ENaC channels at the NMJ immunohistochemically, but we found existing available antibodies to be non-specific *in situ* (Li et al., 2017).

Scnn1a-dependent PHP is induced in TDP-43 and Zfp106 disease models.

We next asked whether Scnn1a-dependent PHP was induced at the degenerating mouse NMJ. First, we asked whether expression of the *Scnn1a* gene was induced in the spinal cord of the *TDP-43* and *Zfp106* mouse models at a stage consistent with ongoing neuromuscular degeneration. We collected the lumbar spinal cord from 4, 8, and 12-week old *Zfp106* knockout and 8-week old *TDP-43* mice and used this as a tissue source for qPCR experiments. We compared expression of the *Scnn1a* gene to identically aged littermate controls. In the *Zfp106* knockout spinal cord, *Scnn1a* gene expression was normal at 4 weeks, a period at which *Zfp106* knockouts are largely presymptomatic. However, *Scnn1a*

gene expression was significantly increased ~ 55% at 8 and 12 weeks, the period during which there is clear neuromuscular degeneration and induction of PHP. Importantly, at 8 weeks in the *TDP-43* model, we observed a surprising 4.6-fold increase in *Scnn1a* transcript when compared to littermate controls (see Supplemental Table S3 for all qPCR values). Because these estimates are averaged across all cell types, they likely under estimate the magnitude of ENaC up-regulation in motoneurons. Thus, in both models, there is evidence for up-regulation of *Scnn1a* transcription that coincides with ongoing neuromuscular degeneration.

If enhanced *Scnn1a* expression mediates PHP in both ALS models, then we should be able to block PHP expression in both ALS models and reveal the full impact of PHP at degenerating NMJ. We applied benzamil (50μM) to the NMJ in wild type and *Zfp106* knockouts (P90), and to *TDP-43* NMJ (P65), ages that represent approximate end stage in each genetic model. As expected, benzamil had no effect on the wild type NMJ. However, benzamil caused a statistically significant decrease in presynaptic release when applied to either the *Zfp106* knockout or the *TDP-43* mutant transgenic (Figure 5A–E). Just as in *Drosophila*, recordings were made from individual NMJ prior to (-Benz) and following acute application of benzamil (+Benz) with lines connecting data points from single NMJ (Figure 5B). Importantly, the recordings were made without prior knowledge of anatomical neurodegeneration. Thus, we observe NMJ that are not affected by benzamil, presumably reflecting intact NMJ. However, the majority of all recordings showed up to a 50% drop in estimated presynaptic release (quantal content, QC) (Figure 5B). The averaged data reveal a statistically significant 25–30% drop in quantal content in both the *Zfp106* knockout and *TDP-43* mutant transgenic NMJ and no change in wild type (Figure 5C).

A more extensive electrophysiological data set is presented for each mutant in which diaphragm muscles were recorded either in the presence or absence of benzamil, but data were not paired (prior to and following application of benzamil; Figure 5D, E). Again, application of benzamil to littermate controls for each genotype was without effect (Figure 5D, F open bars). Application of benzamil to the *TDP-43* mutant transgenic caused a small decrease in mEPP of unknown origin (Figure 5D, green bar, green data points), and a large decrease in EPP amplitude that was associated with a significant decrease in presynaptic quantal content (open/green compared to green/green). A similar set of results was observed in the *Zfp106 KO*. Application of benzamil had no effect on mEPP amplitude (already diminished compared to controls – see also Figure 3). Benzamil caused a significant drop in EPP amplitude and quantal content. Taken together, the experiments in Figure 5 are consistent with the induction of benzamil-dependent PHP in the context of neuromuscular degeneration in two independent mouse models of ALS-like degeneration.

Scnn1a-dependent PHP sustains health-span and lifespan

Having demonstrated that Scnn1a-dependent PHP is induced and expressed at degenerating NMJ in two different mouse models, we had the unique opportunity to test whether genetic elimination of PHP *in vivo* had any effect on neurodegenerative disease onset, progression, behavior or survival. As noted above, the *Scnn1a-CKO* has no substantive neurodegenerative phenotype, consistent with the function of Scnn1a being largely restricted to the induction of

PHP at the NMJ. *Scnn1a-CKO* animals have a normal life span and normal motor behavior (see below). Therefore, by removing the *Scnn1a* gene selectively in motoneurons in a neurodegenerative disease model, we can selectively erase the expression of PHP and, thereby, define the contribution of PHP to disease progression. To do so, we generated double knockout animals (from here forward called DKO) lacking *Scnn1a* in motoneurons (*Scnn1a-CKO*) and harboring a germline knockout for the *Zfp106* gene. We chose the *Zfp106* knockout for these studies because it represents a clear gene deletion, as opposed to the *TDP-43* model that relies on protein over-expression in a transgenic model.

If removing *Scnn1a* blocks PHP in the *Zfp106* knockout background, then we expect to observe a decrease in average EPP amplitude in the DKO (P50) without an offsetting increase in quantal content. This is exactly what we observed. In the control and *Zfp106* single mutants, we found a negative correlation of mEPP and quantal content consistent with robust PHP (Figure 5F). However, in the DKO animals the negative correlation of mEPP and quantal content was abolished (Figure 5F, red data points). Furthermore, the DKO has a reduced average quantal content compared to littermate controls and compared to the single *Zfp106* knockout (Figure 5G) Thus, *Scnn1a*-dependent PHP is necessary in motoneurons for the maintenance of synaptic efficacy in the context of neuromuscular degeneration, at least in the *Zfp106* mutant background.

Given that we can genetically eliminate PHP from the *Zfp106* mutant background, we now have the opportunity to ask what effect this has on animal health. Analysis of animal behavior demonstrated accelerated behavioral decline and early death in double mutants compared to the single *Zfp106* knockout animals (Figure 6). For example, at day P50 the *Zfp106* knockouts remained pre-symptomatic. By contrast, double knockout animals at day P50 showed clear evidence of hind limb and forelimb weakness. Double knockout mice held aloft by their tail were unable to extend their limbs, (Figure 6A; Supplemental Movies 1, 2). Double knockouts also had reduced movement in their home cage compared to age-matched *Zfp106* knockouts (Figure 6C, D). Double knockouts were unable to support themselves on their hind limbs, never rearing to explore or escape when placed in a novel environment, a dramatic difference compared to the age matched single knockout (Figure 6D; Supplemental Movies 3,4). Finally, the lifespan of double knockouts was decreased by 42% compared to the *Zfp106* knockouts. The fifty percent survival rate for the double knockouts was approximately 50 days, whereas the 50% survival rate for *Zfp106* knockouts was approximately 90 days (Figure 6B). As a further control, we also demonstrate that the single *Scnn1a*-CKO animals were phenotypically normal, with a lifespan currently in excess of one year and with no evidence of behavioral differences compared to wild type (Supplemental Figure 4M–O). Thus, early lethality and early onset of behavioral deficits cannot be attributed to simple additive effects of two mutations in the DKO.

Precocious neurodegeneration in the absence of PHP

The profound decrease in DKO lifespan and the early onset of hind limb weakness are quite severe. The absence of homeostatic plasticity should only affect NMJ that are degenerating. At P50, DKO animals are severely impaired, yet degeneration in *Zfp106* knockouts at this time point is relatively modest, suggesting that diminished synaptic gain at degenerating

NMJ is not the only cause of shorted lifespan. Therefore, we sought additional explanations for the severe shift in animal health and lifespan. We hypothesized that loss of PHP might cause a cycle of negative reinforcement, driving precocious neuromuscular degeneration. According to this hypothesis, degeneration might cause a direct loss of synaptic transmission in the absence of PHP. The loss of synaptic transmission would, in turn, lead to more rapid loss of muscle trophic support (or survival factors). Finally, loss of trophic support would lead to more rapid degeneration. This negative feedback cycle might account for the accelerated rate and extent of degeneration and premature death. In support of this hypothesis, we have uncovered evidence of precocious endplate degeneration at the DKO NMJ. At P50, 16% of endplates in the *Zfp106* knockout showed evidence of anatomical degeneration (n=420 NMJ, 3 diaphragms, 3 mice). In contrast, in DKO animals at P50, 54% of endplates showed evidence of anatomical degeneration (n=376 endplates, 3 diaphragms, 3 mice) (Figure 6 F, G).

Given that NMJ anatomy supports our model for precocious neuromuscular degeneration, we sought additional data regarding the rate of neurodegeneration. To do so, we quantified axon number in the phrenic nerve, which innervates the diaphragm muscle, allowing a quantitative assessment of total axon number and, therefore, determination of axon loss. First, we quantified axon number at P30, a stage that is pre-symptomatic in all conditions. There was no change in axon number among genotypes (Figure 7). Next, we quantified axon number at P50-P60, including 1) littermate DKO controls (control), 2) *HB9-Cre* line alone (*HB9-Cre*), 3) *Scnn1a* CKO, 4) *Zfp106* knockout alone (Zfp106), 5) *HB9-Cre* in the *Zfp106* knockout background and 6) the DKO. The DKO had a highly significant decrease in axon number compared to control animals, as well as to *Zfp106* mice (p<0.001) and to *Scnn1a-CKO* alone (one-way ANOVA, p<0.0001, $F_{(5, 23)} = 9.596$). Axon counts were the same in the DKO at P50-P60 as they were in *Zfp106* knockout alone at P90 (p=0.857). These data clearly support our model of precocious neurodegeneration in the absence of PHP.

Further qualitative evidence of precocious axon loss in the *DKO* was evident in representative sections of the phrenic nerve, where axons were misshapen and less densely packed compared to controls, leading to a reduction in nerve diameter. In addition, there were increased numbers of intercalating cells between axons in the DKO phrenic nerve (Figure 7). Again, these data are consistent with the conclusion that there is precocious axon loss and endplate degeneration in the DKO animals compared to controls.

To further address our hypothesis, we sought evidence of accelerated motoneuron loss in the spinal cord and associated activation of an immune response, comparing DKO animals to controls. First, we compared aged controls to *Zfp106* knockouts at P90. This is a readout of the end stage phenotype of *Zfp106* knockouts (Joyce et al., 2016). We found a significant decrease in motoneuron number, an increase in IBA-1 intensity (microglia marker) and an increase in GFAP intensity (astrocyte marker) (Figure 8). Associated with this apparent immune response in the P90 *Zfp106 KO*, we observed a pronounced change in microglia ramification, an indication of microglia activation (see methods) (Figure 8A, D). Specifically, microglia process number and branch number were both significantly decreased by ~50% in the P90 *Zfp106 KO* compared to age-matched controls. When we compared the single mutants (*Scnn1a-CKO* and the *Zfp106* knockout) to the DKO animals at P50, we

found that DKO animals had fewer motoneurons, increased microglia activation, and increased IBA-1 and GFAP intensity (Figure 8). Notably, the values observed in the DKO animals at P50 are statistically similar to those observed in the *Zfp106* knockout at P90, suggesting a shift in neurodegeneration severity of approximately 40 days, providing further evidence for premature degeneration in the *DKO* compared to single mutants.

In summary, double knockouts show a selective failure of PHP, accelerated NMJ degeneration, accelerated motoneuron loss with histological evidence of an immune reaction in the spinal cord, accelerated behavioral decline, and a dramatically shortened lifespan compared to age-matched *Zfp106* knockouts. We conclude that Scnn1a-dependent PHP is a potent form of adaptive physiological compensation that significantly suppresses disease progression in a mouse model of neuromuscular degeneration that may be relevant to ALS pathophysiology.

DISCUSSION

We propose that Scnn1a is a core component necessary for PHP in mammals, just as in *Drosophila*, and that the loss of *Scnn1a* prevents the expression of PHP during neurodegeneration, leading to accelerated disease progression. We refer to this effect as a model of 'homeostatic neuroprotection' (Figure 8H). How might PHP normally slow disease progression in mice? Accelerated disease progression begins at a time when the *Zfp106* knockouts are just entering the phase of active neuronal degeneration. Thus, it seems that beneficial effects of PHP act at the early stages of disease. Several elegant live imaging studies, in mouse and zebrafish, document dynamic neuromuscular remodeling during an early phase of disease whereby denervated endplates can be re-innervated (Schaefer et al., 2005; Martineau et al., 2018). One possibility is that PHP is essential to promote or sustain nascent, re-innervated endplates. Maintaining synaptic gain could sustain activity-dependent, muscle-derived trophic support (Gould and Oppenheim, 2011; Tovar-y-Romo et al., 2014).

There have been experimental and clinical studies attempting to enhance trophic support as a means to suppress neuromuscular degeneration with limited success (Group, 1999; Petrov et al., 2017; but see Held et al., 2019). Several reviews have discussed why trophic factors may have benefit in animal models but fail in human studies (Gould and Oppenheim, 2011; Tovar-y-Romo et al., 2014). One scenario is that enhanced trophic support will be effective only in the early phase of disease, prior to symptom onset (Gould and Oppenheim, 2011; Tovar-y-Romo et al., 2014), a time point that is consistent with an early phase of neuromuscular remodeling and our proposed time of PHP engagement. Consistent with this model, the cellular-basis of degeneration appears to transition from initiation in motoneurons to expression in surrounding glia (Dittsworth et al., 2017; Sun et al., 2015; Taylor et al., 2016). Thus, we predict that the effects of PHP will be disease modifying, not preventative. In this context, mutations that initiate disease and simultaneously impair PHP might cause aggressive forms of disease. A test of this will await further molecular characterization of PHP in mammals. Finally, it seems plausible that the model of homeostatic neuroprotection, described here at the NMJ, could extend to the central nervous system.

Induction of PHP at degenerating neuromuscular synapses

It remains unknown how PHP is induced at degenerating neuromuscular synapses. Previous work at the *Drosophila* NMJ, the mouse NMJ, and human NMJ have shown that diminished postsynaptic neurotransmitter receptor activity or abundance is the cue that induces a homeostatic increase in presynaptic neurotransmitter release. The observed accuracy of PHP, precisely offsetting the magnitude of diminished neurotransmitter receptor function, has led to various hypotheses about the mechanisms of PHP induction, including the action of spontaneous miniature release events or receptor activation itself as a trigger (Davis, 2013, 2006).

At degenerating synapses in *Drosophila*, including the *ank2* mutant (this study) and *Spectrin-RNAi* (Pielage et al., 2005), as well as in *TDP-43* mice (this study), there is no observable change in average mEPP amplitude. Given this observation, how is PHP induced? One possibility is that there is a transient decrease in miniature release event amplitude that occurs during the process of neurodegeneration, as the synapse degenerates. That effect might be sufficient to trigger induction of PHP. Alternatively, stranded neurotransmitter receptors that remain on the muscle surface following the retraction or degeneration of the overlying nerve terminal might initiate the homeostatic response. In either case, a homeostatic response is clearly executed at release sites that remain and the resulting potentiation of release accurately sustains wild type levels of muscle depolarization.

Conservation of mechanism

The phenomenon of PHP is conserved at neuromuscular junctions in organisms ranging from insect to human. To date, the discovery of genes that mediate PHP has occurred solely in *Drosophila*. There are important differences in the NMJ of insects and mammals, highlighted by the fact that insects use glutamate as a neuromuscular neurotransmitter, whereas mammals use acetylcholine. The biochemical composition of the NMJ in insects and mammals are remarkably distinct, as are the mechanisms of excitation-contraction coupling. Thus, it is remarkable that a core mechanism of PHP, the ENaC channel-dependent potentiation of presynaptic release, is precisely conserved from *Drosophila* to mouse, emphasizing that PHP is an ancient regulatory mechanism.

Genetic Context, Disease Progression and the Robustness of PHP

It is well established that genetic context can influence the phenotype and severity of disease causing mutations. Genetic context is one of the factors that may influence the age of onset and progression of ALS (Swinnen and Robberecht, 2014). Experimentally, genetic background has been demonstrated to influence the phenotypic penetrance of neurodegeneration in an Alzheimer's disease model (Ryman et al., 2014). In humans, systematic screening of adults who are phenotypically 'normal' has identified rare individuals who are resilient to the effects of debilitating mutations that confer high risk for devastating childhood disease (Chen et al., 2016). Genetic context can influence many of the processes that are interposed between genotype and phenotype, acting to limit phenotypic penetrance of disease-causing mutations. Our data support the conclusion that PHP acts to limit neuromuscular disease progression. We speculate that some of the variation in disease

onset and progression in human is due not only to the specific disease causing genetic mutation, but also by variation in the robustness of PHP expression due differences in individual genetic background. If so, intervention to promote PHP could have therapeutic value, regardless of the underlying cause of disease, whether inherited or environmental, or a combination of the two.

STAR METHODS

RESOURCE AVAILABILITY

Lead contact—Further information and requests for resources and reagents should be directed to and will be fulfilled by the Lead Contact, Graeme W. Davis (Graeme.Davis@ucsf.edu).

Materials Availability—All unique/stable reagents generated in this study are available from the Lead Contact without restriction.

Data and Code Availability—This study did not generate data sets for public repositories or new data code.

EXPERIMENTAL MODEL AND SUBJECT DETAILS

***Drosophila* stocks and genetics**—All *Drosophila melanogaster* stocks were grown at 22–25°C on normal food, except for the experiments for degeneration mutants including *ank2* mutants, which were grown at room temperature. Both male and female animals were used during experimental procedures. For experiments with *ank2* mutants, 2nd instar homozygous larva were selected from normal food vials and moved to apple plates with yeast paste to facilitate survival. Fly stocks used are: w^{1118} (wild type), $ank2^{2001}$ (Pielage et al., 2008; Spradling et al., 1999), $dcp\text{-}1^{Prev1}$ (Laundrie et al., 2003), and $ank2^{df}$ (Bloomington Stock Center 24399). The $ank2^{2001}$ mutant was maintained as balanced heterozygous mutant strain after outcrossing it to the cantonized w^{1118} background. All experiments were performed in the third instar larva.

Mouse Knockout and genetics—The *Zfp106* allele was generated and bred as previously published (Celona et al., 2017). The *Zfp106* KO was maintained as a heterozygous colony, intercrossed to produce homozygous KO and WT sibling controls. The original *Zfp106* allele was generated on a C57BL/6N Taconic Denmark;C57BL/6J-Tyrc-Brd;C57BL/6N background and outcrossed to an outbred CD-1 background. All data comparisons were made using male and female age matched $Zfp106^{/}$ and $Zfp106^{+/+}$ littermates. Ages are indicated in the text. Genotyping of mutant and transgenic mice was performed by PCR on genomic DNA isolated from tail or ear biopsies using the following primers: *Zfp106*, 5′-caggaggctgtgctgtgata-3′ and 5′-attctaggactgggaggcaga-3′ and 5′-tgaatcagctcgtaaacggac-3′ and 5′-atgaccgctcaaatcgatcaa-3′ for the wild type allele.

The Prp-$TDP43^{A315T}$ mouse line was maintained heterozygous for the mutant $TDP43^{A315T}$ transgene. Heterozygous Prp-$TDP43^{A315T}$ males were bread to *C57BL/6N* females to maintain the colony and generate experimental and control animals. Genotyping of

transgenic mice was performed by PCR on genomic DNA isolated from tail or ear biopsies using the following primers: 5′-ggatgagctgcgggagttct-3′ and 5′-tgcccatcataccccaactg-3′

The *Scnn1a^flox* allele was generated in this study (See CRISPR methods below). We crossed mice harboring this allele with *Mnx1*^Cre/+ (*HB9-Cre*; MGI:109160) line and maintained the colony as heterozygous *Scnn1a^flox/+*; *Mnx1*^Cre/+ animals. Heterozygous animals were bred with mice homozygous for the *Scnn1a^flox* allele to generate homozygous *Scnn1a* CKO. Genotyping of mutant mice was performed by PCR on genomic DNA isolated from tail or ear biopsies using the following primers: Scnn1a 5′ LoxP site, 5′-ttgcacagtcctcctcagtctg-3′ (Primer1) and 5′-ggctcagagaaccggagaagag-3′ (Primer2), Scnn1a 3′ LoxP site genotyping primer 5′-ctagtgcatgggtttagcgtgc-3′ (Primer3) and 5′-ctctatagcacctgcaaggcct-3′ (Primer4), and HB9-Cre 5′-gcggtctggcagtaaaaactatc-3′ and 5′-gtgaaacagcattgctgtcactt-3′.

To generate the ubiquitous KO or neuronal KO of *Scnn1a* for qPCR, we crossed *Scnn1a^flox* allele mice with either *Ndor1*^Tg(UBC-Cre/ERT2)1Ejb mice (MGI:1926047) or Tg(Nes-cre)1Kln (MGI:2176173) line and maintained the colony as heterozygous animals for the *Scnn1a^flox* allele and the Cre driver. Double heterozygous animals were bred with mice homozygous for the *Scnn1a^flox* allele to generate homozygous *Scnn1a* CKO. The following generic Cre PCR primers were used to genotype for the Cre drivers: 5′-gcggtctggcagtaaaaactatc-3′ and 5′-gtgaaacagcattgctgtcactt-3′.

Pregnant mice were administered tamoxifen TM (20 mg/mL; Sigma) to activate tamoxifen inducible Cre driver lines. TM was dissolved in corn oil at E15 and administered at a dose of 2 mg per 30 g of body weight for 5 consecutive days.

To generate the double KO animal (*Zfp106*^/ ; *Scnn1a^flox/flox*; *Mnx1*^Cre/+), we crossed *Scnn1a^flox/+*; *Mnx1*^Cre/+ mice with *Zfp106*^/+ to generate triple heterozygous animals for each allele (*Zfp106*^/+; *Scnn1a^flox/+*; *Mnx1*^Cre/+). We then crossed triple heterozygous mice to mice of the following genotype (*Zfp106*^/+; *Scnn1a^flox/flox*) to generate the double KO animals and appropriate littermate controls.

All animals were matched for age and sex. Experiments conducted in this study were performed on both sexes, with the exception of experiments involving *Prp-TDP43*^A315T mice. We used only males in experiments involving *Prp-TDP43*^A315T mice because previous studies demonstrated that males have a robust neurodegenerative phenotype, unlike the milder, more variable phenotype observed in females. We performed power analyses to determine the sample sizes needed for each experiment. No data collected were excluded from our analysis unless described below, and scientists were not blinded from genotype.

All data were collected in accordance and to the standards with the Institutional Animal Care Use Committee (IACUC) at UCSF. The Animal protocols were approved by IACUC (AN173616–03) on 11/05/2019 and (AN171342–03A) on 07/15/2019. All protocols conform to IACUC approved regulatory standards.

METHOD DETAILS

CRISPR generation of the *Scnn1a* LoxP allele—We generated the Scnn1a flox allele by introducing 2 loxP sites flanking exon 1 (ENSMUSE00000512288) of the Scnn1a gene via CRISPR mediated Homology Directed Repair (HDR). A pBluescript pCR4-TOPO plasmid (Thermo Fisher Scientific) containing the first exon of Scnn1a surrounded by two loxP sites and ~1.2 kb homology arms (donor DNA) and an sgRNA (5'-AAAGTGGTCATGGAGCTGTG-3') targeting a region upstream overlapping of the insertion of first the 3' loxP site (downstream of the exon 1) were co-injected with Cas9 mRNA protein (IDT) into the cytoplasm pronucleus of fertilized mouse oocytes using standard transgenic technology. Two independent F0 founders were independently outcrossed to wild type mice to generate F1 offspring. A single F1 male founder was used to establish a line, which was validated by sequencing across the region surrounding exon 1 and which was subsequently used for Scnn1aflox intercrosses.

Electrophysiology—*Drosophila* electrophysiological recording from the neuromuscular junction: Sharp-electrode recordings were made from muscle 6 in abdominal segments 2 and 3 from third-instar larvae using an Axoclamp 900A amplifier (Molecular Devices), as described previously (Frank et al., 2006; Muller et al., 2012). Recordings were made in HL3 saline containing the following components (in mM) : 70 NaCl, 5 KCl, 10 $MgCl_2$, 10 $NaHCO_3$, 115 sucrose, 5 trehalose, 5 HEPES, and 0.3 $CaCl_2$. Recordings were excluded if the resting membrane potential (RMP) was more depolarized than −55mV. Thirty EPSP traces per muscle were analyzed in IGOR Pro (Wave-Metrics) and with previously published routines in MATLAB (Mathworks) (Ford and Davis, 2014). mEPSP traces were analyzed using MiniAnalysis 6.0.0.7 (Synaptosoft), averaging at least 100 individual mEPSP events. Quantal content was calculated by dividing mean EPSP by mean mEPSP. For acute pharmacological homeostatic challenge, unstretched larvae were incubated in Philanthotoxin-433 (PhTX; 15 μM; Sigma-Aldrich) for 10 min. A threshold 40% decrease in mEPSP amplitude, below average baseline, was used to confirm the efficacy of PhTX incubation. For benzamil experiments, mEPSP and EPSP recordings were first made in a fixed volume of 0.3 mM Ca^{2+} saline. Then, half the volume was removed and replaced by 2x (100 μM) benzamil (benzamil hydrochloride hydrate (Sigma-Aldrich). Benzamil was prepared as a stock in water then diluted to desired concentration. Benzamil recordings were made 5 minutes after benzamil was added, to allow for adequate mixing of benzamil saline. When noted, benzamil was washed out by removing solution and adding fresh saline at least 12 times. Each recording paradigm (i.e. genetic mutant an or treatment) was biologically replicated at least 3 times.

Mouse electrophysiological recording from the neuromuscular junction: Mice (P30-P90 as indicated in text), of both sexes (unless noted as above) were administered isoflurane and euthanized by cervical dislocation. Hemi-diaphragms were recovered from the thoracic cavity, with the phrenic nerve intact. Hemi-diaphragm preparations were placed in a recording chamber and stained with M 4-(4-diethylaminostyryl)-N-methylpyridinium iodide (Invitrogen) to visualize the NMJs. The preparations were perfused at a speed of 3–6 ml/min with an external solution containing the following (in mM): 118 NaCl, 0.7 Mg_2SO_4, 2 $CaCl_2$, 3.5 KCl, 26.2 $NaHCO_3$, 1.7 NaH_2PO_4, and 5.5 glucose, pH 7.3–7.4 (at 20–22°C),

equilibrated with 95% O_2 and 5%CO_2. Contraction of the diaphragm was prevented by the application of 1–3μM conotoxin GIIIB (Peptide Institute, Inc.), which inhibits muscle specific voltage sensitive sodium channels and improves muscle health during recording (Wang et al., 2016). mEPP and EPP intracellular recordings were obtained using single electrode current clamp. D-Tubocurarine was perfused onto the preparation to pharmacologically induce PHP at the mouse NMJ, with a final concentration of 0.1 μm. Benzamil (benzamil hydrochloride hydrate (Sigma-Aldrich) was perfused onto the NMJ preparation at a concentration of 50 μM in order to block ENaC channels at the NMJ. Diaphragms that where incubated in benzamil where simultaneously incubated in conotoxin GIIIB between 30 and 60 minutes. Online recordings from diaphragms before and after benzamil application were perfused for 10 mins with benzamil in external solution to ensure the drug had access to all synapses in the diaphragm. 10 EPPs were recorded and averaged for each NMJ. Multiple endplates were recorded from each hemi-diaphragm and each recording considered a single data point. Each experimental condition was recorded from >3 mice. No collected data was excluded from this study. Best-fit curves for mEPSP amplitude versus quantal content were fit in Prism 6 (GraphPad) using a power function for all wild type data points +/−PhTX. 95% data intervals were fit in IGOR Pro (Wave-Metrics).

Confocal Image acquisition—Low magnification mouse diaphragm or spinal cord images were acquired using a Nikon wide field of view spinning disc confocal. This Nikon system uses Andor Zyla sCMOS Camera to collect data. All low magnification images of the mouse diaphragm were taken using a S Fluor 10x / 0.45 Plan Apo λ or 20x / 0.75 Plan Apo λ Nikon objective. High magnification images of mouse spinal cord were acquired on a Nikon Ti Microscope with a Yokogawa CSU-22 Spinning Disk Confocal system using a Photometrics Evolve Delta EMCCD camera. A Plan Apo VC 60x/1.4 Oil was used. Structured illumination fluorescence microscopy was performed using an N-SIM System (Nikon) with an Apo TIRF 100x/1.49 oil objective on a Ti-E microscope (Nikon) and an Andor DU897 camera. Z-stacks of 120 nm were collected for muscle 4 or 6/7. Images were reconstructed in NIS-Elements 4.12. Maximum projection images were made.

Immunohistochemistry of the NMJ—*Drosophila* immunofluorescence: Standard immunofluorescence was performed as previously described (Pielage et al., 2005). In brief, filleted third instar larvae were fixed in either Bouin's fixative (Sigma-Aldrich, 5 minutes) or ice-cold 100% ethanol. For post-hoc analysis of degeneration severity after electrophysiological recording, preps were stretched and fixed with ethanol in the recording chamber. Preps were washed in PBT (PBS with 0.1% Triton) for 1 hour, then incubated overnight at 4° in primary antibody in PBT. Larval fillets were stained with the following antibodies: mouse anti-BRP (1:100, Developmental Studies Hybridoma Bank (Kittel et al., 2006), rabbit anti-Discs large (Dlg, 1:1,000, (Budnik et al., 1996), and rabbit anti-GlurIIC (Marrus et al., 2004). Preps were washed in PBT for 1 hour and incubated in secondary antibody in PBT for 1 hour at room temperature. Alexa-conjugated secondary antibodies were used at 1:500 and FITC-, Cy3-and Cy5-conjugated HRP was used at 1:100 (Jackson Immuno-research Laboratories) to identify areas of presynaptic degeneration and membrane fragmentation (Keller et al., 2011). Preps were mounted in Vectashield (Vector).

Mouse immunofluorescence: Hemi-diaphragms were collected as described above. Next, tissue was fixed in 2% paraformaldehyde (PFA) for 15 minutes for NMJ morphological analysis. Diaphragms were then washed in 2% PBST for 1 hour to permeabilize the tissue for antibody penetration. Fixed tissue was blocked with 4% normal goat serum for 1 hour in PBST. Diaphragms were incubated over night at 4°C in primary antibodies, washed with 0.1% PBST for 2 hours at room temperature, and incubated at room temperature for 4 hours in secondary antibodies. A final wash was performed in 0.1% PBST for 2 hours. The following primary antibodies were used on mouse tissue: Mouse anti-SV2 monoclonal 1:200 (Hybridoma Bank), Aves anti-Neurofilament-H 1:1000 (Aves Labs, Inc., Catalog # NFH). The following fluorescent conjugated secondary antibodies were used on mouse tissue: goat anti-mouse Alexa Fluor 555 1:500 (Thermo Fisher Scientific), goat anti-chicken 488 1:500 (Aves Labs, Catalog # F-1005), goat anti-Rabbit Alexa Fluor 555 (Thermo Fisher Scientific). To visualize AChR, a far-red fluorophore conjugated to alpha-bungarotoxin Alexa Fluor 680 was used at 1:500 (Thermo Fisher Scientific).

Drosophila NMJ morphological analyses—Quantification of degeneration was performed as previously described (Pielage et al., 2005). Boutons were counted manually at 40x on a Zeiss axioskop compound microscope (40x, 1.1nA lens). Bouton numbers were assessed for type 1b and 1s independently in abdominal segments A2 and A3. Neurodegeneration was assessed in segments A2-A6 with a degenerative event defined as an area of the NMJ with clearly observable postsynaptic DLG staining without any apposing presynaptic BRP staining. Fraction of retracted NMJs (degenerative events) was calculated by dividing number of retractions/ total number of boutons. Vital staining to identify NMJ undergoing degeneration was achieved by incubation in Cy3-conjugated HRP at 1:1000, applied to dissected NMJ at room temperature in HL3 saline followed by repeated washes in HL3 for up to ten minutes prior to NMJ electrophysiology.

Immunohistochemistry of the mouse spinal cord—Immunohistochemical characterization of postnatal control, single mutants and double mutants was performed at indicated ages. For the analysis of CNS histopathology, spinal cords were fixed by transcardial perfusion with 4% paraformaldehyde, followed by overnight post-fixation at 4°C. All tissues were cryoprotected in 30% sucrose. 20 μm cryostat sections from the lumbar region of fixed spinal cords were collected onto glass slides and immuno-fluorescently stained with anti-GFAP (Cy-conjugated mouse monoclonal, Sigma; 1:1000) and anti-IBA1 (rabbit polyclonal, Abcam; 1:500), visualized using a secondary AlexaFluor 488-conjugated antibody (Invitrogen) and counterstained with NeuroTrace® 435/455 fluorescent Nissl stain (Invitrogen). All primary and secondary antibodies were diluted in PBS containing 10% goat serum and 0.3% Triton X-100. Sections were coverslipped with Vectashield (Vector labs). All data points in figure 8 were collected from the following number of animals from each genotype and age: Control P90 (2 animals). _Zfp106_ KO P90 (2 animals), _Scnn1a-CKO_ P60 (3 animals), Zfp106 KO P60 (2 animals), Double KO (4 animals).

Microglia analysis—Spinal cord images were analyzed according to standard procedures developed by current experts in the field of reactive glia biology (Guo et al., 2013; Joyce et

al., 2016; Young and Morrison, 2018). First, we quantified integrated fluorescence intensity of IBA-1 staining in the ventral horn of the lumbar spinal cord across experimental genotypes and age matched sibling controls using imageJ integrated intensity measurements in the Measure Module. This quantification was performed on images collected using 20X objective on the Nikon wide field of view spinning disc confocal (see Image acquisition above).

IBA-1 staining in the spinal cord defines microglia cell bodies and their processes within the ventral horn. We took 100X images of the microglia and characterized their branch number, branch complexity, and cell shape. First, we generated a 2 dimensional skeletons of microglia using the Analyze Skeleton plugin in ImageJ (Young and Morrison, 2018). This data was generated from a 3D Z-stack of imaged collected with a 100x objective on a Kokogawa CSU-22 Spinning Disk Confocal system (see above). This skeleton representation of the microglia shape allows us to count microglia processes and branching point number of these processes. When microglia are activated, they retract their processes to focus around a point of interest. This change in activation can be quantified by a reduction in in microglia complexity and branch number. We quantified branch number if microglia in each experimental genotype and age matched sibling controls.

Astrocyte analysis—We quantified integrated fluorescence intensity of GFAP staining in the ventral horn of the lumbar spinal cord across genotypes and age matched sibling controls using imageJ integrated intensity measurements in the Measure Module. This quantification was performed on images collected using 20X objective on the Nikon wide field of view spinning disc confocal (see Image acquisition above)(Joyce et al., 2016).

Alpha motor neuron analysis—We counted alpha motor neurons across experimental genotypes and age match controls using Nissl staining of the ventral horn of the spinal cord. Alpha motor neurons where identified according to their previously defined cellular area (nuclear diameter >9–10 μm; cell body diameter >20 mm) and anatomical hallmarks (Guo et al., 2013; Lance-jones, 1982).

CNS Quantitative RT-PCR—RT-PCR was performed as previously described (Celona et al., 2017; Younger et al., 2013). For *Drosophila*, the CNS was removed from 5 third-instar larvae per sample (three samples/genotype). Total RNA was isolated from each sample using the RNeasy Plus Micro Kit (Qiagen), then DNase treated with TURBO DNA-free (Ambion). cDNA was synthesized using the SuperScript III First-Strand synthesis system (Invitrogen). qPCR was done with the TaqMan kit (Thermo Fischer) with six technical replicates per sample. For *Drosophila*, *ppk11/16* and *rpl32* primers were from Applied Biosystems.

Primer probes for real-time PCR detection of Scnn1a and Hprt (hypoxanthine phosphoribosyltransferase 1) were designed and developed by IDT, Integrated DNA Technology. RNA was isolated from the cortices of 3 adult mice *Scnn1a*$^{flox/flox}$; *Nestin-Cre*$^{Tg/0}$ and 2 adult mice *Scnn1a*$^{+/+}$; *Nestin-Cre*$^{Tg/0}$ using RNeasy Plus Micro Kit (Qiagen). RNAs were DNAse-treated and purified with TURBO DNA-free (Ambion). RNA was reverse-transcribed into cDNA with SuperScript III First-Strand synthesis system (Invitrogen). A no reverse transcriptase (RT) control was included for each sample. Purified

cDNA was used as a template in PCR reaction with three technical replicates for each condition (TaqMan Fast Universal PCR Master Mix, no AmpErase UNG, Applied Biosystems). Additionally, a no RT reaction was included for each sample. Primer information are reported in key resource table. Cycle Threshold (CT) was determined by automated threshold analysis using SDS2.4 software (Applied Biosystems, Foster City, CA). Relative expression values were determined using the CT method. This same procedure was used in our analysis of *Scnn1a* expression in models of ALS. We define the experimental ALS animals as homozygous *Zfp106* KO and hemizygous transgenic *Prp-TDP43*[A315T] animals compared to their wild type littermates.

Electron microscopy—Phrenic nerves were prepared for electron microscopy by trans-cardiac perfusion of mice previously anaesthetized with Isoflurane using 50–70 ml 2.5% glutaraldehyde/2% formaldehyde in PO_4 buffer, pH 7.4. Following perfusion, the phrenic nerves were excised and placed in fresh fixative for 1 hour of additional fixation at room temperature. Intact nerves were then rinsed in buffer, post-fixed with 1% OsO_4/1.5% $KFe(CN)_6$ in 0.1M Na-cacodylate buffer, pH 7.4, for 1 hour followed by 1% OsO_4 in 0.1M Na-cacodylate buffer for 1 hour at room temperature. The nerves were then rinsed in water, *en bloc* stained with 5% uranyl acetate in water, dehydrated in ethanol followed by propylene oxide and embedded in Eponate 12 resin (Ted Pella, Redding, CA). Thin sections were cut with a Leica UCT ultramicrotome using a Diatome diamond knife, picked up on carbon coated Pioloform films on slot grids, and stained with 5% uranyl acetate followed by Sato's lead (Sato, 1968). Sections were examined and photographed on an FEI T12 TEM (Hillsborough, OR) operated at 120 kV using a Gatan U895 4k camera. Quantification of axon numbers in the phrenic nerve was done by counting axon cross-sections from electron micrographs, across experimental genotypes and ages matched controls. A one-way ANOVA with multiple comparisons was performed on this data set to determine groups statistically different from the data set.

Mouse lifespan—Using a power analysis, we determined that at $\alpha=0.05$ and 80% power, we can detect a 50% change in lifespan using 4 mice, both male and female. However, we were more conservative and used at least 8 mice in each condition. The following genotypes were analyzed for lifespan: 1) *Scnn1a*[flox/flox]; *Mnx1*[Cre/+], 2) *Zfp106*[/], and 3) *Zfp106*[/]; *Scnn1a*[flox/flox]; *Mnx1*[Cre/+]. Mutant mice were housed as all other mice in the study, in cages of 3 to 5 animals. Once a mouse reached a body conditioning score of 2, it was humanely euthanized.

Mobility assay—Mouse mobility was recorded using an iPhone (Apple Inc. Cupertino, CA) with the following settings: 4K resolution, 30 frames per second (fps). Recordings were made in .MOV file format and opened in Fiji with the QuickTime Opener plugin. Recordings were done between 2:00 PM and 5:00 PM. *Zfp106*[/] and *Zfp106*[/]; *Scnn1a*[flox/flox]; *Mnx1*[Cre/+] mice were recorded for 5 mins in their home cage. We ran our analysis of these data on Mac Book pro running macOS 10.14 operating system, using Fiji (version 2.0.0). The RAM size of 16 GB was sufficient to process the 30 fps videos up to 5 minutes. Videos were analyzed with Fiji with imageJ plugin wrMTrck, developed by Jesper Søndergaard Pedersen.

QUANTIFICATION AND STATISTICAL ANALYSIS

All bar graphs display data as mean values. The error bars represent standard error of the mean (SEM). Statistical analysis was performed using Prism (5.01, GraphPad) and using paired two-tailed Student's t test or one-way ANOVA as indicated in the figure legends. A one-way ANOVA was used when comparing across multiple groups. Statistical details for comparison can be found in the figure legends. In each experiment, >6 NMJs were recorded from across 3 or more animals in each condition. Experimental sample sizes equal to or greater than 6 were considered sufficiently powered to detect a significant change between groups, an effect of size of ~80–120% compared to controls.

Supplementary Material

Refer to Web version on PubMed Central for supplementary material.

ACKNOWLEDGEMENTS

REFERENCES

Anderson DM, Cannavino J, Li H, Anderson KM, Nelson BR, McAnally J, Bezprozvannaya S, Liu Y, Lin W, Liu N, Bassel-Duby R, Olson EN (2016). Severe muscle wasting and denervation in mice lacking the RNA-binding protein ZFP106. Proc. Natl. Acad. Sci. U. S. A 113, E4494–503. [PubMed: 27418600]

Arber S, Han B, Mendelsohn M, Smith M, Jessell TM, Sockanathan S (1999). Requirement for the homeobox gene Hb9 in the consolidation of motor neuron identity. Neuron 23, 659–674. [PubMed: 10482234]

Bose P, Armstrong GAB, Drapeau P (2019). Neuromuscular junction abnormalities in a zebrafish loss-of-function model of TDP-43. J Neurophysiol. 121, 285–297. [PubMed: 30461368]

Dzieciolowska S, Drapeau P, Armstrong GAB (2017). Augmented quantal release of acetylcholine at the vertebrate neuromuscular junction following tdp-43 depletion. PLoS One 12, e0177005. [PubMed: 28472174]

Budnik V, Koh YH, Guan B, Hartmann B, Hough C, Woods D, Gorczyca M (1996). Regulation of synapse structure and function by the Drosophila tumor suppressor gene dlg. Neuron 17, 627–640. [PubMed: 8893021]

Celona B, Von Dollen J, Vatsavayai SC, Kashima R, Johnson JR, Tang AA, Hata A, Miller BL, Huang EJ, Krogan NJ, Seeley WW, Black BL (2017). Suppression of C9orf72 RNA repeat-induced neurotoxicity by the ALS-associated RNA-binding protein Zfp106. Elife 6, e19032. [PubMed: 28072389]

Chand KK, Lee KM, Lee JD, Qiu H, Willis EF, Lavidis NA, Hilliard MA, Noakes PG. (2018) Defects in synaptic transmission at the neuromuscular junction precede motor deficits in a TDP-43Q331K transgenic mouse model of amyotrophic lateral sclerosis. FASEB J. 32, 2676–2689. [PubMed: 29295857]

Chen R, Shi L, Hakenberg J, Naughton B, Sklar P, Zhang J, Zhou H, Tian L, Prakash O, Lemire M, Sleiman P, Cheng W, Chen W, Shah H, Shen Y, Fromer M, Omberg L, Deardorff MA, Zackai E, Bobe JR, Levin E, Hudson TJ, Groop L, Wang J, Hakonarson H, Wojcicki A, Diaz GA, Edelmann L, Schadt EE, Friend SH (2016). Analysis of 589,306 genomes identifies individuals resilient to severe Mendelian childhood diseases. Nat. Biotechnol 34, 531–538. [PubMed: 27065010]

Cook C, Petrucelli L. (2019) Genetic Convergence Brings Clarity to the Enigmatic Red Line in ALS. Neuron 101, 1057–1069. [PubMed: 30897357]

Cull-Candy SG, Miledi R, Trautmann A, Uchitel OD (1980). On the release of transmitter at normal, myasthenia gravis and myasthenic syndrome affected human end-plates. J. Physiol 299, 621–638. [PubMed: 6103954]

Davis GW (2013). Homeostatic Signaling and the Stabilization of Neural Function. Neuron 80, 718–728. [PubMed: 24183022]

Davis GW (2006). Homeostatic control of neural activity: from phenomenology to molecular design. Annu. Rev. Neurosci 29, 307–323. [PubMed: 16776588]

Ditsworth D, Maldonado M, McAlonis-Downes M, Sun S, Seelman A, Drenner K, Arnold E, Ling SC, Pizzo D, Ravits J, Cleveland DW, Da Cruz S. (2017) Mutant TDP-43 within motor neurons drives disease onset but not progression in amyotrophic lateral sclerosis. Acta Neuropathol. 133, 907–922. [PubMed: 28357566]

Dyka FM, May CA, Enz R (2005). Subunits of the epithelial sodium channel family are differentially expressed in the retina of mice with ocular hypertension. J. Neurochem 94, 120–128. [PubMed: 15953355]

Eaton BA, Fetter RD, Davis GW (2002). Dynactin is necessary for synapse stabilization. Neuron 34, 729–741. [PubMed: 12062020]

Estes PS, Daniel SG, McCallum AP, Boehringer AV, Sukhina AS, Zwick RA, Zarnescu DC. (2013) Motor neurons and glia exhibit specific individualized responses to TDP-43 expression in a Drosophila model of amyotrophic lateral sclerosis. Dis Model Mech. 6, 721–33. [PubMed: 23471911]

Fearnley JM, Lees AJ (1991). Ageing and Parkinson's disease: substantia nigra regional selectivity. Brain 114, 2283–301. [PubMed: 1933245]

Figley MD, Gitler AD. (2013) Yeast genetic screen reveals novel therapeutic strategy for ALS. Rare Dis. 1:e24420 [PubMed: 25002991]

Filipchuk AA, Durand J. (2012) Postnatal dendritic development in lumbar motoneurons in mutant superoxide dismutase 1 mouse model of amyotrophic lateral sclerosis. Neuroscience 209,144–54. [PubMed: 22387111]

Ford KJ, Davis GW (2014). Archaerhodopsin voltage imaging: synaptic calcium and BK channels stabilize action potential repolarization at the Drosophila neuromuscular junction. J. Neurosci 34, 14517–25. [PubMed: 25355206]

Frank CA, Kennedy MJ, Goold CPC, Marek KW, Davis GW (2006). Mechanisms Underlying the Rapid Induction and Sustained Expression of Synaptic Homeostasis. Neuron 52, 663–677. [PubMed: 17114050]

Giraldez T, Domínguez J, Alvarez de la Rosa D (2013). ENaC in the brain--future perspectives and pharmacological implications. Curr. Mol. Pharmacol 6, 44–9. [PubMed: 23547934]

Gitcho MA, Baloh RH, Chakraverty S, Mayo K, Norton JB, Levitch D, Hatanpaa KJ, White CL, Bigio EH, Caselli R, Baker M, Al-Lozi MT, Morris JC, Pestronk A, Rademakers R, Goate AM, Cairns NJ, Cairns NJ (2008). TDP-43 A315T mutation in familial motor neuron disease. Ann. Neurol 63, 535–8. [PubMed: 18288693]

Graf ER, Heerssen HM, Wright CM, Davis GW, DiAntonio A. (2011) Stathmin is required for stability of the Drosophila neuromuscular junction. J Neurosci. 31, 15026–34. [PubMed: 22016536]

Gould TW, Oppenheim RW. (2011) Motor neuron trophic factors: therapeutic use in ALS? Brain Res Rev. 67, 1–39. [PubMed: 20971133]

Group, T.B.S. (1999). A controlled trial of recombinant methionyl human BDNF in ALS. Neurology 52.

Guo J, Qiu W, Soh SLY, Wei S, Radda GK, Ong W, Pang ZP, Han W (2013). Motor neuron degeneration in a mouse model of seipinopathy. Cell Death Dis. 4, e535–11. [PubMed: 23470542]

Held A, Major P, Sahin A, Reenan RA, Lipscombe D, Wharton KA. (2019) Circuit Dysfunction in SOD1-ALS Model First Detected in Sensory Feedback Prior to Motor Neuron Degeneration Is Alleviated by BMP Signaling. J Neurosci. 39, 2347–2364. [PubMed: 30659087]

Hummler E, Barker P, Gatzy J, Beermann F, Verdumo C, Schmidt A, Boucher R, Rossier BC, (1996). Early death due to defective neonatal lung liquid clearance in αENaC-deficient mice. Nat. Genet 12, 325–328. [PubMed: 8589728]

Joyce PI, Fratta P, Landman AS, Mcgoldrick P, Wackerhage H, Groves M, Busam BS, Galino J, Corrochano S, Beskina OA, Esapa C, Ryder E, Carter S, Stewart M, Codner G, Hilton H, Teboul L, Tucker J, Lionikas A, Estabel J, Ramirez-solis R, White JK, Brandner S, Plagnol V, Bennet DLH, Abramov AY, Greensmith L, Fisher EMC, Acevedo-arozena A (2016). Deficiency of the zinc fi nger protein ZFP106 causes motor and sensory neurodegeneration. Hum. Mol. Genet 25, 291–307. [PubMed: 26604141]

Keller LC, Cheng L, Locke CJ, Müller M, Fetter RD, Davis GW (2011). Glial-Derived Prodegenerative Signaling in the Drosophila Neuromuscular System. Neuron 72, 760–775. [PubMed: 22153373]

Klim JR, Williams LA, Limone F, et al. (2019) ALS-implicated protein TDP-43 sustains levels of STMN2, a mediator of motor neuron growth and repair. Nat Neurosci. 22, 167–179. [PubMed: 30643292]

Kittel RJ, Wichmann C, Rasse TM, Fouquet W, Schmidt M, Schmid A, Wagh DA, Pawlu C, Kellner RR, Willig KI, Hell SW, Buchner E, Heckmann M, Sigrist SJ, (2006). Bruchpilot Promotes Active Zone Assembly, Ca2+ Channel Clustering, and Vesicle Release. Science 312, 1051–1054. [PubMed: 16614170]

LaMonte BH, Wallace KE, Holloway BA, Shelly SS, Ascaño J, Tokito M, Van Winkle T, Howland DS, Holzbaur EL. (2002) Disruption of dynein/dynactin inhibits axonal transport in motor neurons causing late-onset progressive degeneration. Neuron 34, 715–27. [PubMed: 12062019]

Lance-jones C (1982). Motoneuron Cell Death in the Developing Lumbar Spinal Cord of the Mouse. Dev. Brain Res 4, 473–479.

Laundrie B, Peterson JS, Baum JS, Chang JC, Fileppo D, Thompson SR, McCall K, (2003). Germline cell death is inhibited by P-element insertions disrupting the dcp-1/pita nested gene pair in Drosophila. Genetics 165, 1881–8. [PubMed: 14704173]

Li Y, Chang J, Cui Y, Zhao R, Ding Y, Hou Y (2017). Novel mechanisms for crotonaldehyde-induced lung edema. Oncotarget 8, 83509–83522. [PubMed: 29137360]

Marrus SB, DiAntonio A (2005). Investigating the safety factor at an invertebrate neuromuscular junction. J. Neurobiol 63, 62–69. [PubMed: 15685612]

Marrus SB, Portman SL, Allen MJ, Moffat KG, DiAntonio A (2004). Differential Localization of Glutamate Receptor Subunits at the Drosophila Neuromuscular Junction. J. Neurosci 24, 1406–1415. [PubMed: 14960613]

Martineau É, Di Polo A, Vande Velde C, Robitaille R. (2018) Dynamic neuromuscular remodeling precedes motor-unit loss in a mouse model of ALS. Elife 7 pii: e41973. [PubMed: 30320556]

Massaro CM, Pielage J, Davis GW (2009). Molecular mechanisms that enhance synapse stability despite persistent disruption of the spectrin/ankyrin/microtubule cytoskeleton. J. Cell Biol 187, 101–117. [PubMed: 19805631]

McGurk L, Berson A, Bonini NM. (2015) Drosophila as an In Vivo Model for Human Neurodegenerative Disease. Genetics 201, 377–402. [PubMed: 26447127]

Melamed Z, López-Erauskin J, Baughn MW, Zhang O, Drenner K, Sun Y, Freyermuth F, McMahon MA, Beccari MS, Artates JW, Ohkubo T, Rodriguez M, Lin N, Wu D, Bennett CF, Rigo F, Da Cruz S, Ravits J, Lagier-Tourenne C, Cleveland DW (2019). Premature polyadenylation-mediated loss of stathmin-2 is a hallmark of TDP-43-dependent neurodegeneration. Nat. Neurosci 22, 180–190. [PubMed: 30643298]

Moloney EB, de Winter F, Verhaagen J (2014). ALS as a distal axonopathy: molecular mechanisms affecting neuromuscular junction stability in the presymptomatic stages of the disease. Front. Neurosci 8, 252. [PubMed: 25177267]

Morrison JH, Baxter MG (2012). The ageing cortical synapse: hallmarks and implications for cognitive decline. Nat. Rev. Neurosci 13, 240–250. [PubMed: 22395804]

Müller M, Davis GW (2012). Transsynaptic control of presynaptic Ca 2+ influx achieves homeostatic potentiation of neurotransmitter release. Curr. Biol 22, 1102–1108. [PubMed: 22633807]

Muller M, Liu KSY, Sigrist SJ, Davis GW (2012). RIM Controls Homeostatic Plasticity through Modulation of the Readily-Releasable Vesicle Pool. J. Neurosci 32, 16574–16585. [PubMed: 23175813]

Neumann M, Sampathu DM, Kwong LK, Truax AC, Micsenyi MC, Chou TT, Bruce J, Schuck T, Grossman M, Clark CM, McCluskey LF, Miller BL, Masliah E, Mackenzie IR, Feldman H, Feiden W, Kretzschmar HA, Trojanowski JQ, Lee VM-Y (2006). Ubiquitinated TDP-43 in frontotemporal lobar degeneration and amyotrophic lateral sclerosis. Science 314, 130–3. [PubMed: 17023659]

Orr BO, Gorczyca D, Younger MA, Jan LY, Jan Y-N, Davis GW (2017). Composition and Control of a Deg/ENaC Channel during Presynaptic Homeostatic Plasticity. Cell Rep. 20, 1855–1866. [PubMed: 28834749]

Petel Légaré V, Harji ZA, Rampal CJ, Allard-Chamard X, Rodríguez EC, Armstrong GAB. (2019) Augmentation of spinal cord glutamatergic synaptic currents in zebrafish primary motoneurons expressing mutant human TARDBP (TDP-43). Sci Rep. 9, 9122. [PubMed: 31235725]

Perry S, Han Y, Das A, Dickman D (2017). Homeostatic plasticity can be induced and expressed to restore synaptic strength at neuromuscular junctions undergoing ALS-related degeneration. Hum. Mol. Genet 26, 4153–4167 [PubMed: 28973139]

Peters A, Sethares C, Luebke JI (2008). Synapses are lost during aging in the primate prefrontal cortex. Neuroscience 152, 970–81. [PubMed: 18329176]

Petrov D, Mansfield C, Moussy A, Hermine O (2017). ALS Clinical Trials Review: 20 Years of Failure. Are We Any Closer to Registering a New Treatment? Front. Aging Neurosci 9, 68. [PubMed: 28382000]

Pielage J, Cheng L, Fetter RD, Carlton PM, Sedat JW, Davis GW (2008). Article A Presynaptic Giant Ankyrin Stabilizes the NMJ through Regulation of Presynaptic Microtubules and Transsynaptic Cell Adhesion. Neuron 58, 195–209. [PubMed: 18439405]

Pielage J, Fetter RD, Davis GW, Francisco S (2005). Presynaptic Spectrin Is Essential for Synapse Stabilization. Curr. Biol 15, 918–928. [PubMed: 15916948]

Plomp JJ, van Kempen GT, Molenaar PC (1992). Adaptation of quantal content to decreased postsynaptic sensitivity at single endplates in alpha bungarotoxin treated rats. J. Physiol 458, 487–499. [PubMed: 1302275]

Price DL, Cleveland DW, Koliatsos VE. (1994) Motor neurone disease and animal models. Neurobiol Dis. 1, 3–11. [PubMed: 9216981]

Ryman DC, Aisen PS, Bird T, Danek A, Fox NC, Goate A, Frommelt P, Langbaum JBS, Martins R, Masters CL, Mayeux RP, Mcdade E, Moreno S, Reiman EM, Ringman JM, Salloway S, Morris JC, Bateman RJ (2014). Symptom onset in autosomal dominant Alzheimer disease A systematic review and meta-analysis Neurology. 83, 253–260. [PubMed: 24928124]

Sato T, (1968). A modified method for lead staining of thin sections. J. Electron Microsc. (Tokyo) 17, 158–9. [PubMed: 4177281]

Schaefer AM, Sanes JR, Lichtman JW. (2005) A compensatory subpopulation of motor neurons in a mouse model of amyotrophic lateral sclerosis. J Comp Neurol. 490, 209–19. [PubMed: 16082680]

Sons MS, Verhage M, Plomp JJ (2003). Role of Munc18–1 in Synaptic Plasticity at the Myasthenic Neuromuscular Junction. Ann. N. Y. Acad. Sci 998, 404–6. [PubMed: 14592907]

Spradling AC, Stern D, Beaton A, Rhem EJ, Laverty T, Mozden N, Misra S, Rubin GM, (1999). The Berkeley Drosophila Genome Project gene disruption project: Single P-element insertions mutating 25% of vital Drosophila genes. Genetics 153, 135–77. [PubMed: 10471706]

Starr A, Sattler R. (2018) Synaptic dysfunction and altered excitability in C9ORF72 ALS/FTD. Brain Res. 1693 (Pt A), 98–108. [PubMed: 29453960]

Sun S, Sun Y, Ling SC, et al. (2015) Translational profiling identifies a cascade of damage initiated in motor neurons and spreading to glia in mutant SOD1-mediated ALS. Proc Natl Acad Sci U S A. 112, E6993–E7002. [PubMed: 26621731]

Swinnen B, Robberecht W (2014). The phenotypic variability of amyotrophic lateral sclerosis. Nat. Rev. Neurol 10, 661–670. [PubMed: 25311585]

Taylor JP, Brown RH Jr, Cleveland DW. (2016) Decoding ALS: from genes to mechanism. Nature 539, 197–206. [PubMed: 27830784]

Teruyama R, Sakuraba M, Wilson LL, Wandrey NEJ, Armstrong WE (2012). Epithelial Na$^+$ sodium channels in magnocellular cells of the rat supraoptic and paraventricular nuclei. Am. J. Physiol. Metab 302, E273–E285.

Tovar-Y-Romo LB, Ramírez-Jarquín UN, Lazo-Gómez R, Tapia R. (2014) Trophic factors as modulators of motor neuron physiology and survival: implications for ALS therapy. Front Cell Neurosci. 8, 61. [PubMed: 24616665]

Tremblay E, Martineau É, Robitaille R. (2017) Opposite Synaptic Alterations at the Neuromuscular Junction in an ALS Mouse Model: When Motor Units Matter. J Neurosci. 37,8901–8918. [PubMed: 28821658]

Van Deerlin VM, Leverenz JB, Bekris LM, Bird TD, Yuan W, Elman LB, Clay D, Wood EM, Chen-Plotkin AS, Martinez-Lage M, Steinbart E, McCluskey L, Grossman M, Neumann M, Wu I-L, Yang W-S, Kalb R, Galasko DR, Montine TJ, Trojanowski JQ, Lee VM-Y, Schellenberg GD, Yu C-E (2008). TARDBP mutations in amyotrophic lateral sclerosis with TDP-43 neuropathology: a genetic and histopathological analysis. Lancet. Neurol 7, 409–16. [PubMed: 18396105]

Wang X, Pinter MJ, Rich MM, (2016). Reversible Recruitment of a Homeostatic Reserve Pool of Synaptic Vesicles Underlies Rapid Homeostatic Plasticity of Quantal Content. J. Neurosci 36, 828–36. [PubMed: 26791213]

Wegorzewska I, Bell S, Cairns NJ, Miller TM, Baloh RH (2009). TDP-43 mutant transgenic mice develop features of ALS and frontotemporal lobar degeneration. Proc. Natl. Acad. Sci. U. S. A 106, 18809–14. [PubMed: 19833869]

Young K, Morrison H (2018). Quantifying Microglia Morphology from Photomicrographs of Immunohistochemistry Prepared Tissue Using ImageJ. J. Vis. Exp 136.

Younger MA, Müller M, Tong A, Pym EC, Davis GW (2013). A Presynaptic ENaC Channel Drives Homeostatic Plasticity. Neuron 79, 1183–1196. [PubMed: 23973209]

Yuva-Aydemir Y, Almeida S, Gao FB. (2018) Insights into C9ORF72-Related ALS/FTD from Drosophila and iPSC Models. Trends Neurosci. 41, 457–469. [PubMed: 29729808]

Highlights:

1. In *Drosophila* and mouse, NMJ degeneration induces homeostatic plasticity.

2. Deletion of *Scnn1a* in motoneurons blocks homeostatic plasticity at the mouse NMJ.

3. *Scnn1a* cKO causes precocious disease progression in an ALS-like mutant background.

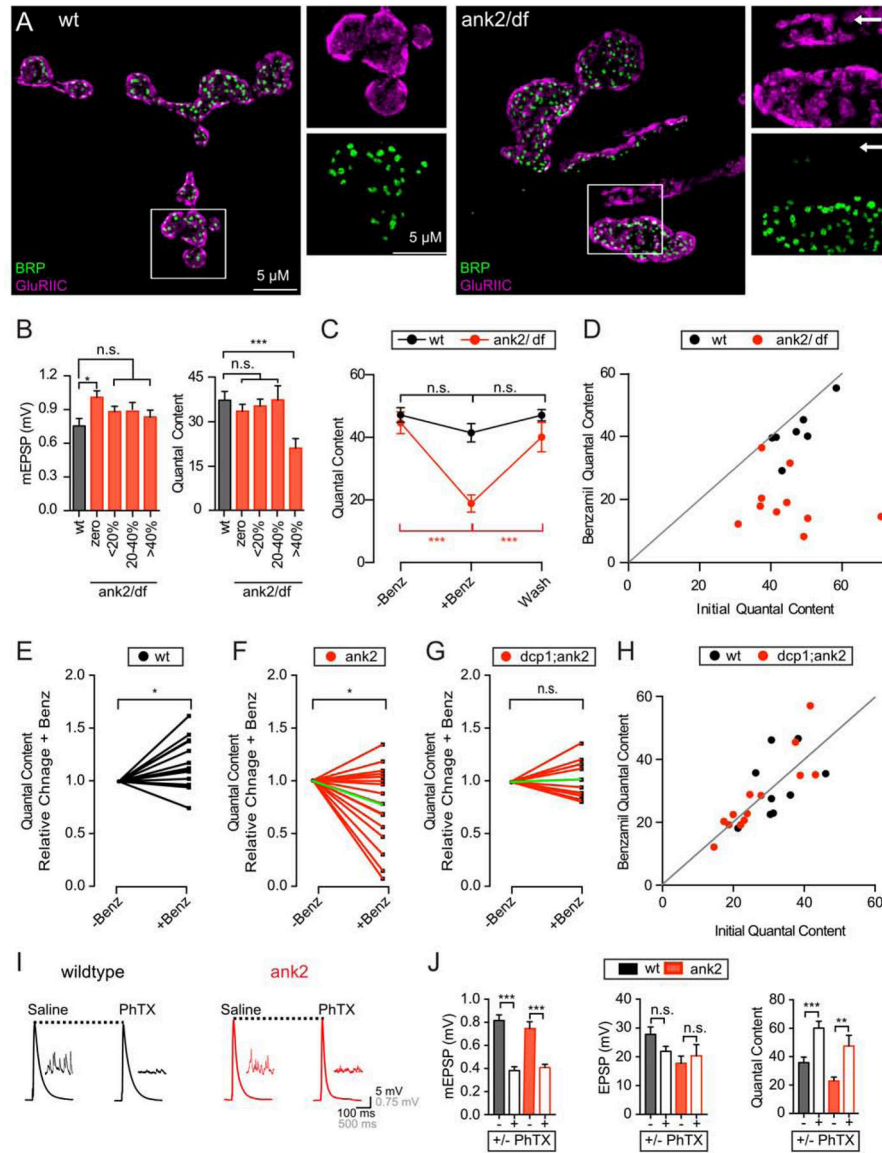4. A model of 'homeostatic neuroprotection' is proposed.

Figure 1. Degeneration induces presynaptic homeostatic plasticity at the *Drosophila* NMJ.
(**A**) Representative images (muscle 4 NMJ),, insets as indicated. In *ank2/df* (right), the arrow indicates an area of degeneration. (**B**) Average data for wild type (black) and *ank2²⁰⁰¹/df* (red), binned according to degeneration severity. One-way ANOVA followed by Dunnet Test comparing each mutant sub-category to wild type. (**C**) Average data for NMJ recorded prior to (−Benz), following benzamil (+Benz) and after washout (Wash). One-way ANOVA for each genotype with Tukey's multiple comparisons. (**D**) Each point represents a single NMJ prior to (x-axis) and following benzamil application (y-axis). The grey line represents unity. (**E-G**) Normalized data for individual NMJ recordings assessed prior to (-Benz) and following (+ Benz) benzamil application. Lines connect data from single NMJ. Green lines represent the population average. (**H**) Data as in (D) for wild type (black) and the double mutant *dcp1;ank2* (red). (**I**) Representative traces. (**J**) Solid bars indicate no PhTx (−PhTX),

open bars indicated presence of PhTx (+PhTX). Student's *t*-test. NS not significant, * p<0.01. Recordings at 0.3 mM $[Ca^{2+}]_e$. Data represent mean ± SEM
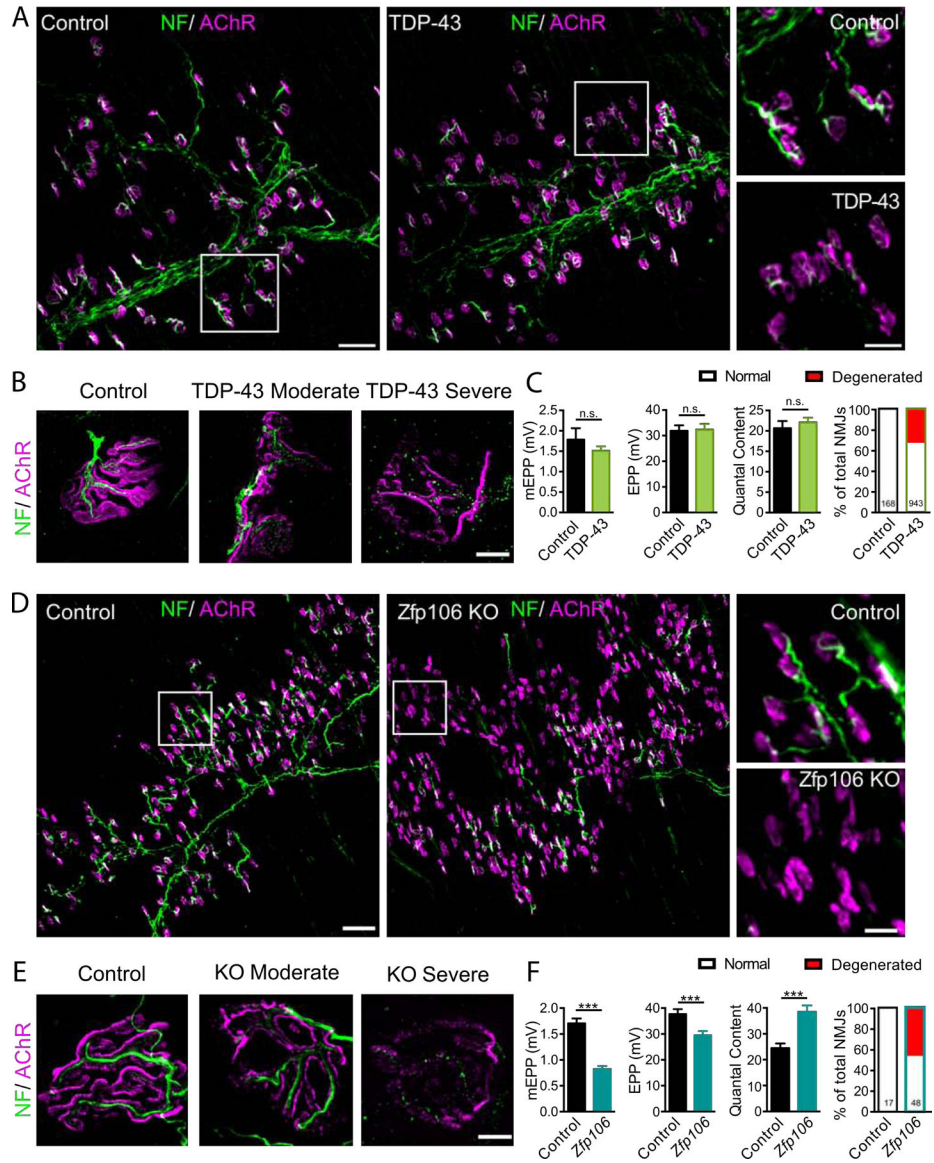
Figure 2. NMJ degeneration in *TDP-43^A315T* and *Zfp106* diaphragm muscle.
(A and D) Representative images of diaphragm for indicated genotypes labeled for
Neurofilament (NF, Green) and postsynaptic acetylcholine receptors (AChR, magenta).
Scale bar is 140μm. Insets indicated by white box with scale bar of 20μm. **(B and E)** NMJ
as in (A) for control, *TDP-43^A315T* mutant transgenic and *Zfp106* KO. Scale Bar is 10μm.
(C and F) Average data for electrophysiological recordings as indicated. *TDP-43^A315T*
(P65-P70) and *Zfp106* (P90-P100). Far right graph shows % anatomical degeneration.
Students *t*-Test, two-tailed. NS not significant, * p<0.05, ** p<0.01, *** p<0.001.
Recordings at 2 mM [Ca^2+]_e. Data represent mean ± SEM. See also Supplemental Figures
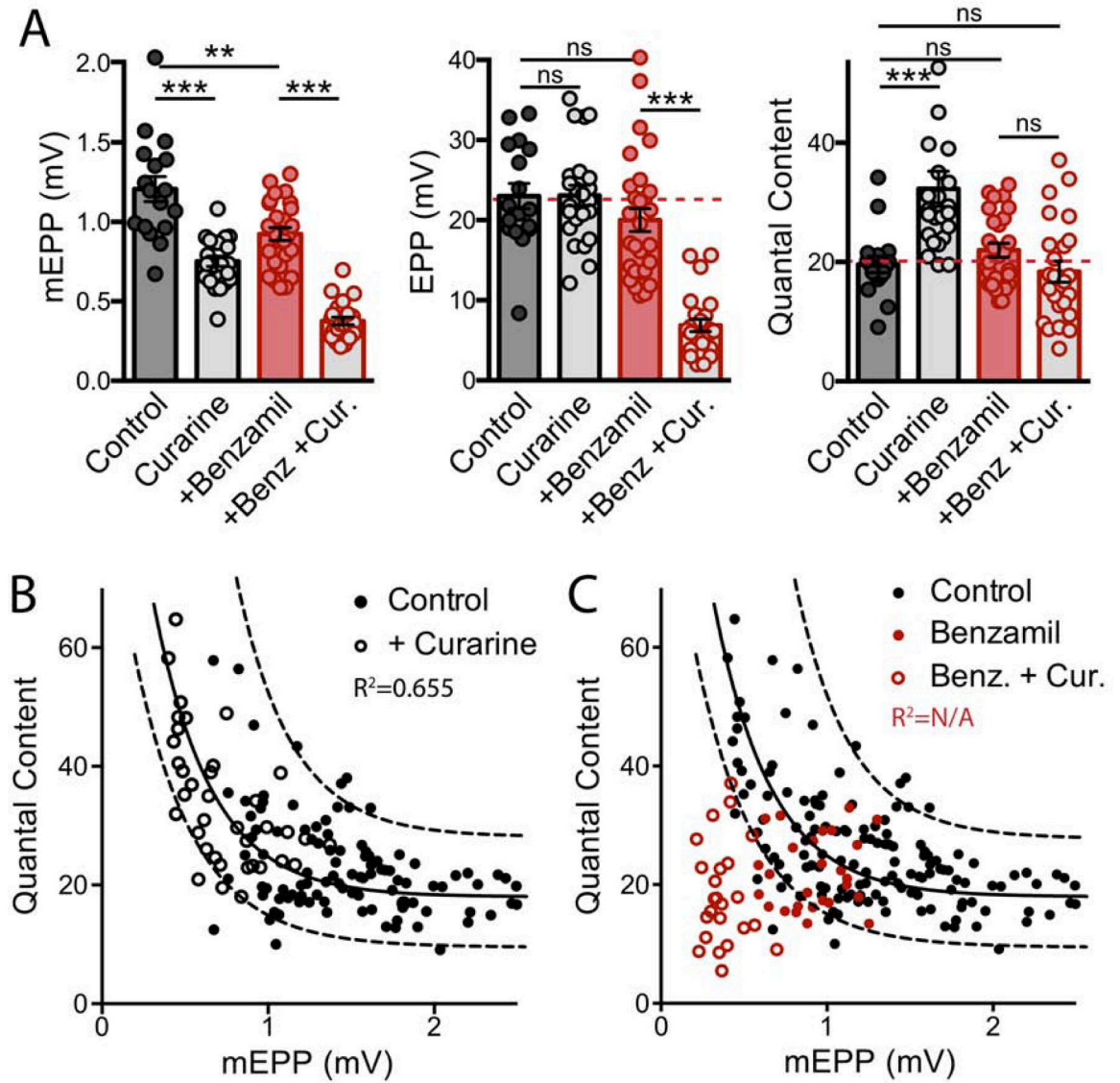S1–S4.

Figure 3. The ENaC antagonist benzamil blocks PHP at the mouse diaphragm NMJ.
(A) Average values for wild type (*C57BL/6J* at P90) for conditions: no drug (control), following curarine application (+Curarine), following benzamil application (+Benzamil) or co-application of both drugs (+Benz +Cur.). **(B and C)** Each data point represents a single NMJ recording for wild type (*C57BL/6J*) in the absence (control; black) and presence of curarine (+Curarine; open). (B) The dotted lines encompass 95% of all control data and the solid black represents the line of best fit for control data +/− curarine. (C) Data from wild type (presented in B) with addition of recordings made in the presence of benzamil (solid red) or co-application of benzamil and curarine (Benz + Cur.). Students *t*-Test, two-tailed. NS not significant, * p<0.05, ** p<0.01, *** p<0.001. Recordings at 2 mM [Ca^{2+}]$_e$. In panel (C), designation of N/A indicates that no line could be fit to the data.
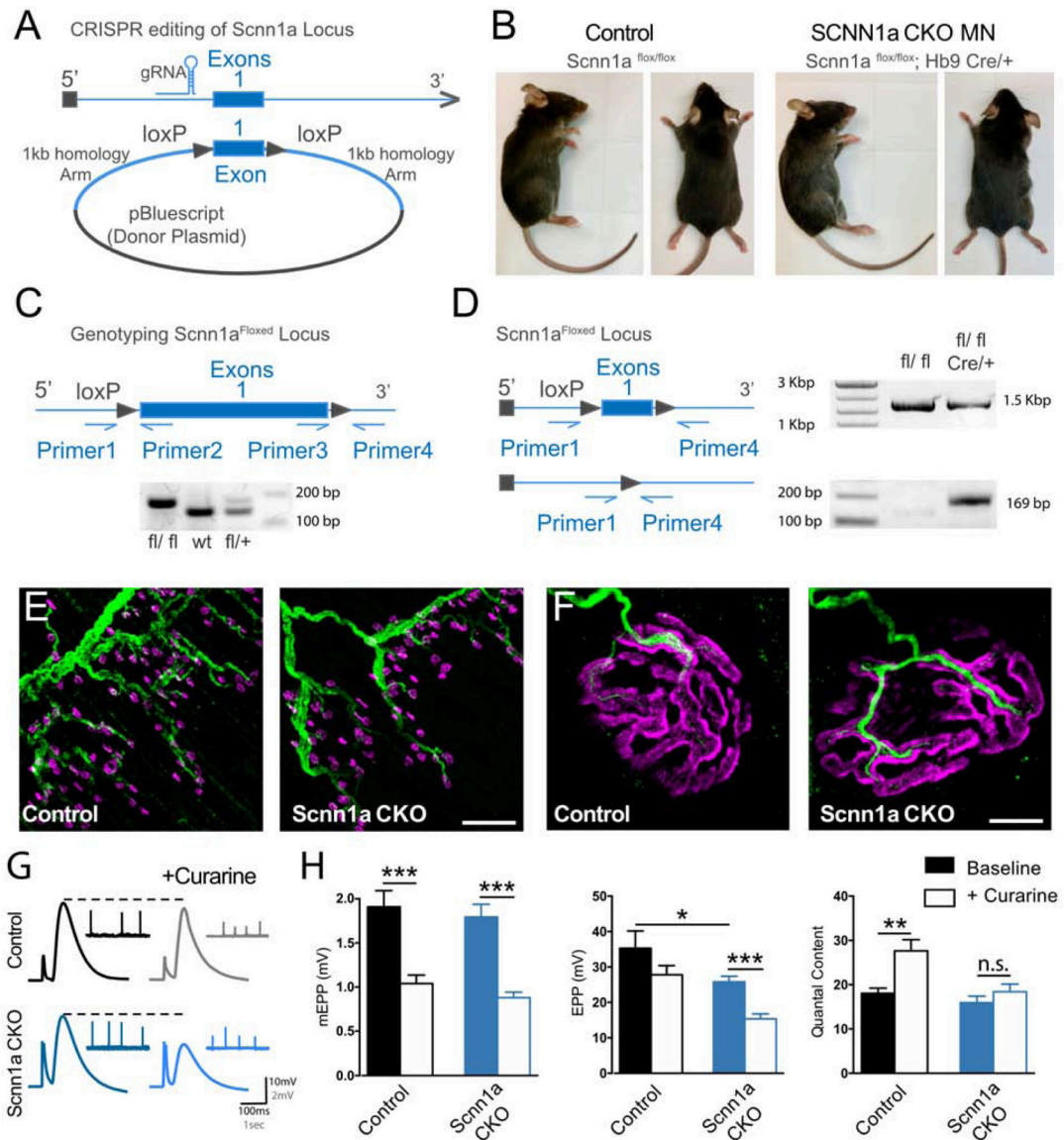
Figure 4. *Scnn1a* motoneuron conditional knockout blocks PHP.
(A) Schematic of CRISPR induced *Scnn1a* LoxP allele. A single guide RNA was used to direct a double stranded break in the DNA upstream of first exon of the *Scnn1a* locus. The 1st exon of the *Scnn1a* locus with 5' and 3' flanking LoxP sites and 1kb homology arms were cloned to direct the insertion of LoxP sites during homology directed repair. **(B)** Representative images of homozygous *Scnn1a* LoxP allele and *Scnn1a CKO*. **(C)** Schematic for the genotyping rationale and PCR based genotyping results. PCR product for primers 1 and 2 amplify a 145bp fragment of DNA and a larger 179bp fragment when the LoxP site is present in the 5' region upstream of the 1st exon. PCR product for primers 3 and 4 amplify a 143bp fragment of DNA and a larger 177bp fragment when the LoxP site is present in the 3' region downstream of the 1st exon. **(D)** Schematic for removal of the *Scnn1a* first exon and resulting PCR amplicons . We used Primers 1 and 4 to amplify 1.5 Kbp fragment of DNA across the 1st exon. This fragment is reduced to 169 bp following exon removal. **(E)** Images

of NMJ in control *Scnn1a CKO*. Scale Bar represents 100μm. **(F)** Images of individual motoneuron endplates. Scale bar represents 10μm. **(G)** Representative traces. **(H)** Average data (2 mM $[Ca^{2+}]_e$) for homozygous *Scnn1a* LoxP allele and homozygous *Scnn1a* LoxP allele in combination with *HB9*-Cre. Data represent mean ± SEM. * p<0.05, ** p<0.01, *** p<0.001. NS indicates not significant. Students *t*-Test, two-tailed. Recordings at 2 mM $[Ca^{2+}]_e$. See also Supplemental Figure 4.
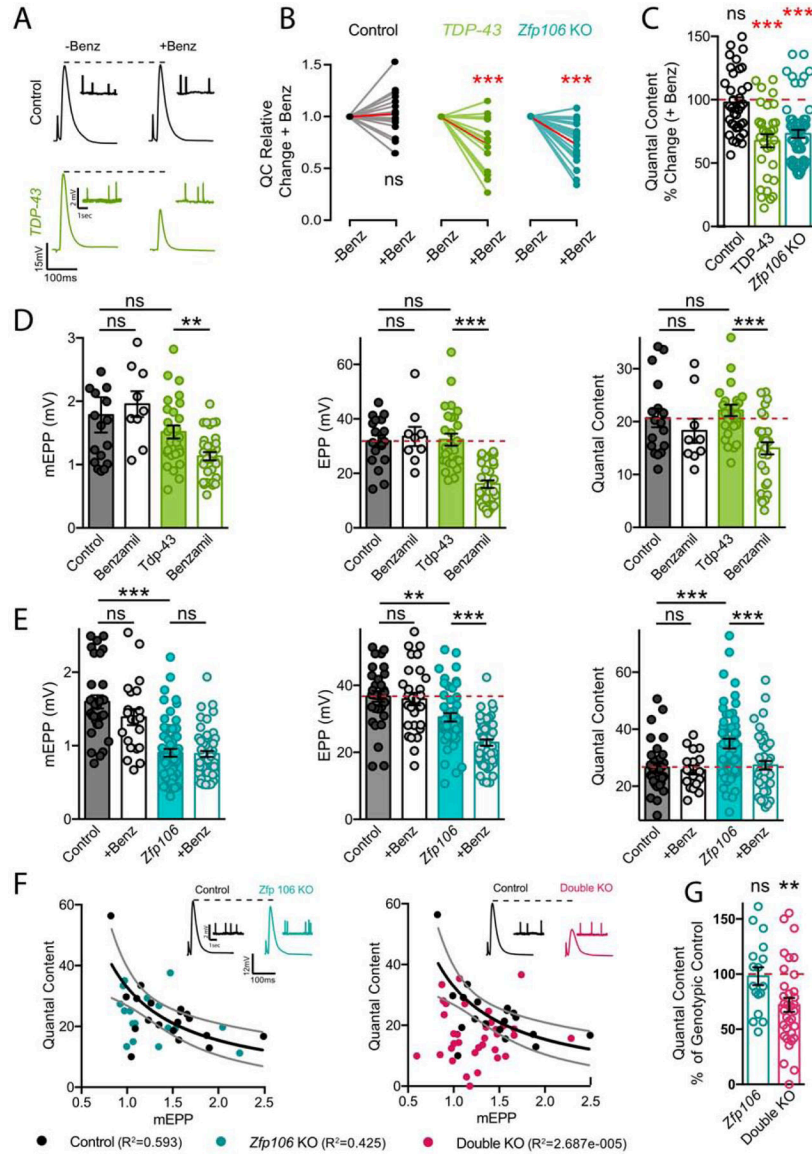
Figure 5. Scnn1a dependent PHP is induced in two models of neurodegeneration
(A) Representative traces in the absence (-Benz) and presence (+Benz) of benzamil. **(B)** Normalized data for individual mouse NMJ recordings prior to (-Benz) and following (+Benz) benzamil application. Lines connect data from single NMJ. Red lines represent population average. **(C)** Data for indicated genotypes ± Benz. **(D and E)** Genotypes indicated by color with closed bars (-Benz) and open bars (+Benz). **(F)** Each point represents an NMJ recording for the indicated genotypes (P50). Gray lines encompass 95% of the control dataset. The solid black is the line of best fit for control data. Control data are the same in each graph with indicated mutant data over-layered. Representative traces are shown. **(G)** Normalized data for recordings in (F). Data displayed as percent change compared to control (age matched sibling). Data represent mean ± SEM. * $p < 0.05$, ** $p < 0.01$, *** $p < 0.001$. NS indicates not significant. Students *t*-Test, two-tailed. Recordings at 2 mM $[Ca^{2+}]_e$. See also Supplemental Figure 4.
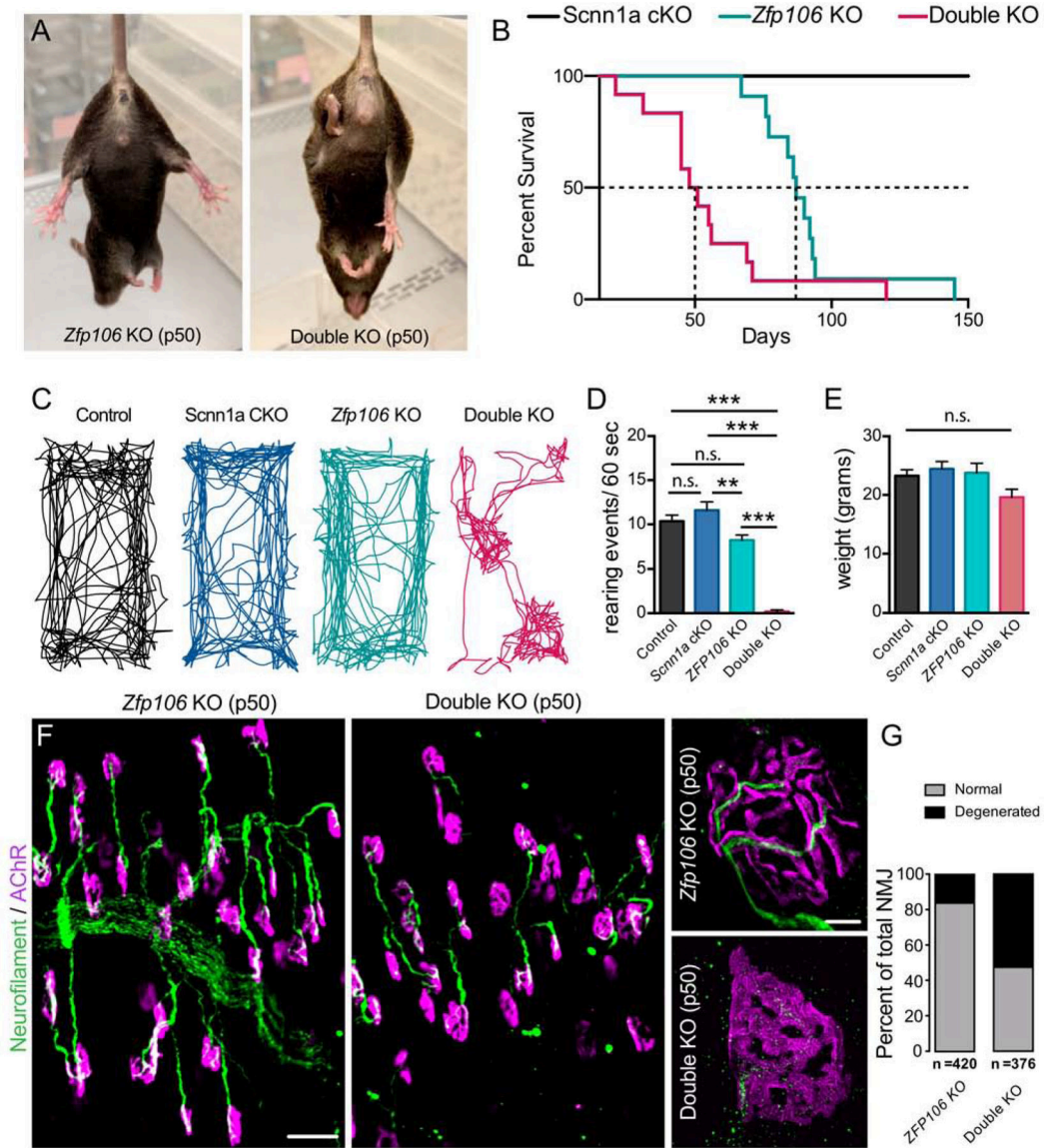
Figure 6. Scnn1a dependent PHP extends lifespan in a model of neurodegeneration.
(A) Representative images of limb extension behavior; see also Supplemental Movies 1 and 2. **(B)** Percent survival plot for indicated genotypes. Double KO animals (n=12) exhibit shortened lifespan compared to homozygous *Zfp106* KO (n=11) and *Scnn1a* cKO (n=21). **(C)** Representative tracking of mouse mobility. **(D)** Mean rearing events per 60 second interval (P50) (standing on hind limbs; see also Supplemental Movies 3, 4). Sample size   6 animals per genotype, 4 trials per animal. **(E)** Mean weight at P50. Sample sizes: Control (n=6), *Double KO* (n=9), *Zfp106* KO (n=6) and *Scnn1a* cKO (n=6). **(F)** Representative images of NMJ. Scale bar represents 20μm and 5μm for inset. **(G)** Quantification of neurodegeneration. * p<0.05, ** p<0.01, *** p<0.001. Data represent mean ± SEM. * p<0.05, ** p<0.01, *** p<0.001. NS indicates not significant. Students *t*-Test, two-tailed. See also Supplemental Figure 4.
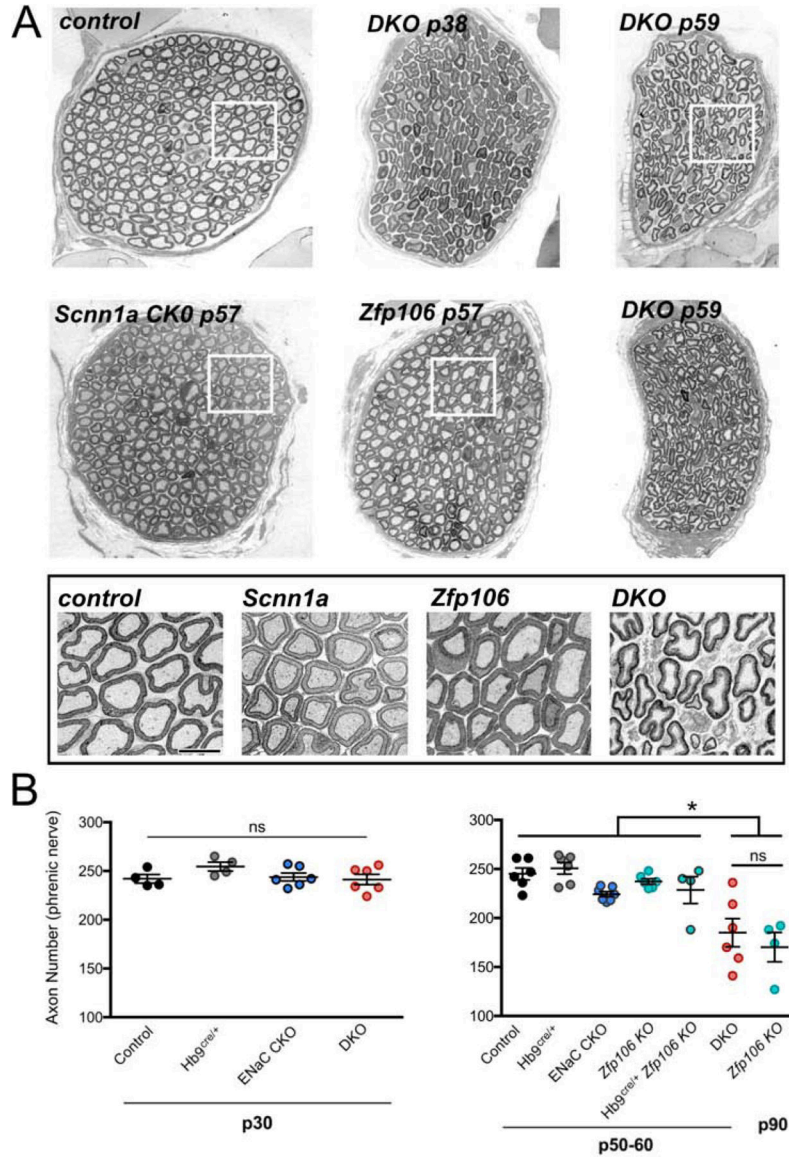
Figure 7. Precocious axon loss in DKO phrenic nerve.

(A) Representative cross-sectional images of phrenic nerve for indicated genotypes and ages. White boxes correspond to the insets below. Scale 10μm. **(B)** Average number of axons counted per nerve for indicated genotypes at corresponding ages. Asterisk represents p-value < 0.05. NS indicates not significant (One-way ANOVA with multiple comparisons). Additional comparisons and p-values as follows: *DKO* vs. *control* (p<0.001), *DKO* vs. *HB9Cre/+* (p<0.001), *DKO* vs. *Scnn1a CKO* (p<0.05), *DKO* vs. *Zfp106 KO* (p<0.001), *DKO* vs. *Zfp106 KO* with *Hb9Cre/+* (p<0.01). Sample sizes (number of nerves) and mean ± SEM indicated on graph (* p<0.05).
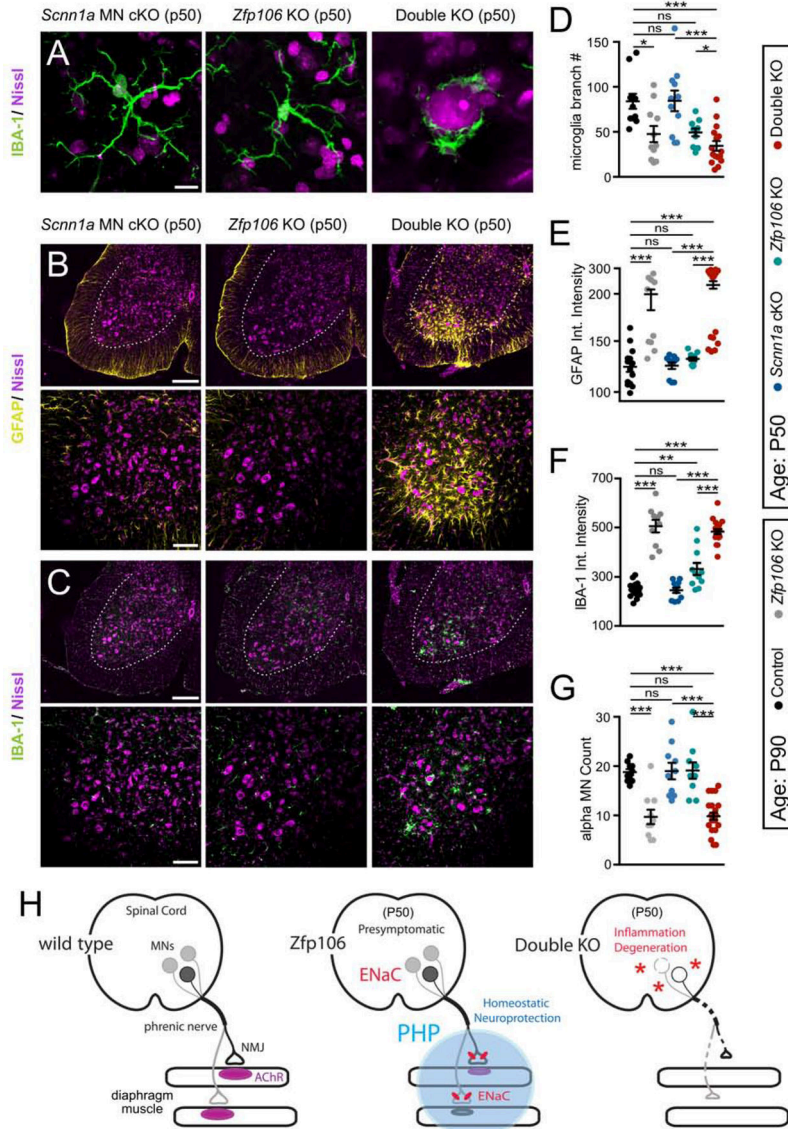
Figure 8. Precocious inflammatory response and MN death: Model of homeostatic neuroprotection.

(A) Representative images of ventral horn with IBA-1 (microglial marker) in green and Nissl in magenta. Scale bar 10μm. **(B)** Images of ventral horn with GFAP in yellow (astrocyte marker) and Nissl in magenta. Scale bar 200μm, inset 50μm. **(C)** Images of ventral horn with IBA-1 (microglial marker) in green and Nissl in magenta. Scale bar represents 200μm, inset is 50μm. **(D-G)** Quantification of microglial branching (D), GFAP intensity (E), IBA-1 intensity (F) and alpha motor neuron counts (G) for genotypes and ages listed at right. Data represent mean ± SEM. * p<0.05, ** p<0.01, *** p<0.001. NS indicates not significant. Students *t*-Test, two-tailed. **(H)** Model of homeostatic neuroprotection. Diagram of spinal cord, motoneurons, phrenic nerve and NMJ of diaphragm muscle in wild type (left), *Zfp106KO* (middle) and the *DKO* (right). Presynaptic homeostatic plasticity (PHP) is induced during degeneration in the *Zfp106 KO* (blue cloud). Local expression of PHP sustains gain of neurotransmission at the NMJ via insertion and function of presynaptic

ENaC channels (red ovals). The induction of PHP is neuroprotective in the context of degeneration, including diminished postsynaptic acetylcholine receptors at individual endplates (smaller purple ovals). In the DKO, PHP fails to be expressed, resulting in precocious neuromuscular degeneration. Degeneration is observed locally at the NMJ and at the level of motoneuron number and axon number in nerve and spinal cord

KEY RESOURCES TABLE

REAGENT or RESOURCE	SOURCE	IDENTIFIER
Antibodies		
mouse anti-Bruchpilot (1:100)	Developmental Studies Hybridoma Bank	Cat #: Nc82; RRID: AB_2314866
rabbit anti-GlurIIC	DiAntonio Lab; Marrus and DiAntonio 2004	RRID: AB_2568754
Mouse anti-SV2 (1:200)	Developmental Studies Hybridoma Bank	Cat #: SV2 RRID: AB_2315387
Aves anti-Neurofilament-H (1:1000)	Aves Labbs,INC.	Cat #: NFH RRID: AB_2313552
Alexa Fluor® 488 AffiniPure Goat Anti-Mouse IgG (H+L)	Jackson Immuno-research Laboratories	Cat #:115-545-003 RRID: AB_2338840
Cy™3 AffiniPure Goat Anti-Mouse IgG (H+L)	Jackson Immuno-research Laboratories	Cat #:115-165-003 RRID: AB_2338680
Alexa Fluor® 488 AffiniPure Goat Anti-Rabbit IgG (H+L)	Jackson Immuno-research Laboratories	Cat #:111-545-003 RRID: AB_2338046
Cy™3 AffiniPure Goat Anti-Rabbit IgG (H+L)	Jackson Immuno-research Laboratories	Cat #:111-165-003 RRID: AB_2338000
Alexa Fluor® 488 AffiniPure Goat Anti-Horseradish Peroxidase (1:100)	Jackson Immuno-research Laboratories	Cat #:123-545-021 RRID: AB_2338965
Cy™3 AffiniPure Goat Anti-Horseradish Peroxidase	Jackson Immuno-research Laboratories	Cat #:123-165-021 RRID: AB_2338959
Alexa Fluor® 647 AffiniPure Goat Anti-Horseradish Peroxidase	Jackson Immuno-research Laboratories	Cat #:123-605-021 RRID: AB_2338967
α-Bungarotoxin, Alexa Fluor™ 467 conjugate	ThermoFisher Scientific	Cat # B35450
α-Bungarotoxin, Alexa Fluor™ 555 conjugate	ThermoFisher Scientific	Cat # B35451
NeuroTrace 435⁄455 fluorescent Nissl	Invitrogen	Cat # N21479
IBA-1 Antibody (1:500)	Abcam	Cat # ab5076 RRID:N/A
anti-GFAP Cy3-conjugated mouse monoclonal (1:1000)	Sigma	Cat # C9205 RRID:N/A
Chemicals, Peptides, and Recombinant Proteins		
Philanthotoxin-433	Santa Cruz Biotechnology	Cat# 255421, CAS 276684-27-6
M 4-(4-diethylaminostyryl)-N-methylpyridinium iodide	Invitrogen	Cat # D288
conotoxin GIIIB	Peptide Institute, Inc.	Cat # 4217-v
D-Tubocurarine	Sigma Aldrich	Cat # T2379
Benzamil hydrochloride hydrate	Sigma Aldrich	Cat # B2417

REAGENT or RESOURCE	SOURCE	IDENTIFIER
Tamoxifen	Sigma Aldrich	Cat # 10540-29-1
Experimental Models: Organisms/Strains		
w^{1118} (*Drosophila*)	Bloomington	BDSC: 19062
ank2 ^{2001} (*Drosophila*)	Bloomington	BDSC: 18502
dcp-1 ^{Prev1} (*Drosophila*)	Bloomington	BDSC: 63814
ank2 ^{df} (*Drosophila*)	Bloomington	BDSC: 24399
Zfp106 KO (*Mus musculus*)	Brian Black Lab UCSF	N/A
Scnn1a LoxP (*Mus musculus*)	This Manuscript	N/A
Mnx1$^{Cre/+}$ (*Mus musculus*)	Jackson Lab	JAX: 006600 MGI:109160
Prp-Tdp-43^{A315T} (*Mus musculus*)	Jackson Lab	JAX: 010700 MGI:4358722
Tg(Nes-cre)1Kln (*Mus musculus*)	Jackson Lab	JAX: 003771 MGI:2176173
Ndor1$^{Tg(UBC-cre/ERT2)1Ejb}$	Jackson Lab	JAX: 007001 MGI:1926047
Oligonucleotides		
Primers for genotyping see Table S4		
ppk11/16 qPCR primer	ThermoFischer/ Applied Biosystems	Dm02151827_g1 Cat # 4351372
Rpl32 qPCR primer	ThermoFischer	Dm02151827_g1 Cat # 4331182
Scnn1a qPCR primer	Taqman Applied Biosystems	Mm00803386_m1 Cat # 4453320
Gdaph qPCR primer	Taqman Applied Biosystems	Mm99999915_g1 Cat # 4453320
Scnn1a gRNA Sequence GAAGGAGGATAACTTCGTATAGCATACATTATACGAAGTTATATCGCCGAGAGTAGG	This paper	N/A
Software and Algorithms		
GraphPad Prism (5.01)	GraphPad	http://www.graphpad.com/ scientific-software/prism/
MiniAnalysis (6.0.3)	Synaptosoft	http:// www.synaptosoft.com/ MiniAnalysis/
Igor Pro (6.37)	WaveMetrics	https:// www.wavemetrics.com/ software/igor-pro-637- installer
Fiji	NIH	https://imagej.net/Fiji/ Downloads
SlideBook	Intelligent Imaging Innovation	https://www.intelligent- imaging.com/slidebook

REAGENT or RESOURCE	SOURCE	IDENTIFIER
Axon™pCLAMP™ 10	Molecular Devices	http://mdc.custhelp.com/app/answers/detail/a_id/18779/~/axon™pclamp™-10-electrophysiology-data-acquisition-%26-analysis-software-download
Axon™Clampfit™ 10	Molecular Devices	http://mdc.custhelp.com/app/answers/detail/a_id/18779/~/axon™pclamp™-10-electrophysiology-data-acquisition-%26-analysis-software-download